universität wien

MASTERARBEIT | MASTER'S THESIS

Titel | Title

Snowball Earth and waterbelt states in ExoCAM

verfasst von | submitted by

Anatol Waba BSc

angestrebter akademischer Grad | in partial fulfilment of the requirements for the degree of

Master of Science (MSc)

Wien | Vienna, 2024

Studienkennzahl lt. Studienblatt | Degree programme code as it appears on the student record sheet:	UA 066 614
Studienrichtung lt. Studienblatt | Degree programme as it appears on the student record sheet:	Masterstudium Meteorology
Betreut von | Supervisor:	Univ.-Prof. Dr. Aiko Voigt

Abstract

Waterbelt states play a crucial role in enhancing the survivability of life on a planet under extreme conditions such as Snowball events, providing a vital refuge amidst harsh environmental challenges.

This thesis explores the dynamics of Snowball Earth, which most likely occurred at least three times in Earth's history, focusing on identifying the geological plausibility of waterbelt states using the ExoCAM climate model. These waterbelt states represent an alternative to a Snowball Earth scenario with globally frozen oceans. I investigate the existence and characteristics of these climate states through simulations, confirming stable waterbelt states and identifying critical bifurcation points across varying atmospheric CO_2 levels. Comparative analyses with other climate models reveal diverse representations and dependencies on model properties. Compared to previous studies using the CAM and ICON climate models, ExoCAM exhibits an expanded range of radiative forcing with a stable waterbelt state. The interruption of the ice-albedo runaway feedback is essential for stabilizing the ice edge in the tropics. Enhanced reflectivity of snow-covered sea ice, in comparison to the albedo of open ocean, would otherwise lead to a Snowball bifurcation with globally frozen oceans. In ExoCAM, the reduced reflectivity of bare sea ice near the ice edge stabilizes the system in the waterbelt state, where the average ice edge is found at approximately $\pm 15^\circ$ latitude. This stable waterbelt state in ExoCAM occurs within atmospheric CO_2 concentrations ranging from 45 to 8000 ppmv. The onset of transition from a temperate, ice-free state is found at 1400 ppmv CO_2, highlighting the geological plausibility of the waterbelt state in ExoCAM.

The analysis of ExoCAM simulations reveals the characteristics of waterbelt states, encompassing precipitation, evaporation, seasonal ice coverage, albedo, the impact of clouds on incoming solar radiation and top-of-the-atmosphere energy balance. Furthermore, the thesis includes a comprehensive installation guide for ExoCAM on high-performance computer systems.

Zusammenfassung

Wassergürtelzustände spielen eine entscheidende Rolle bei der Verbesserung der Überlebensfähigkeit von Leben auf einem Planeten unter extremen Bedingungen wie Schneeballereignissen und bieten inmitten harter Umweltbedingungen einen wichtigen Zufluchtsort.

Diese Arbeit untersucht die Dynamik der Schneeballerde, die wahrscheinlich mindestens dreimal in der Geschichte der Erde auftrat, mit dem Schwerpunkt auf der Identifizierung der geologischen Plausibilität von Wassergürtelzuständen unter Verwendung des ExoCAM-Klimamodells. Diese Wassergürtelzustände stellen eine Alternative zu einem Szenario der Schneeballerde mit global gefrorenen Ozeanen dar. Durch Simulationen untersuche ich die Existenz und die Merkmale dieser Klimazustände, bestätige stabile Wassergürtelzustände und identifiziere kritische Bifurkationspunkte bei variierenden Konzentrationen von atmosphärischem CO_2. Vergleichsanalysen mit anderen Klimamodellen zeigen unterschiedliche Darstellungen und Abhängigkeiten von Modellparametern auf. Im Vergleich zu früheren Studien mit den Klimamodellen CAM und ICON zeigt ExoCAM einen erweiterten Bereich des Strahlungsantriebs mit einem stabilen Wassergürtelzustand. Die Unterbrechung des Eis-Albedo-Rückkopplungseffekts ist entscheidend für die Stabilisierung der Eiskante in den Tropen. Die erhöhte Reflexivität von schneebedecktem Meereis, im Gegensatz zur Albedo des offenen Ozeans, würde andernfalls zu einer Schneeballerde-Bifurkation mit global gefrorenen Ozeanen führen. In ExoCAM stabilisiert die reduzierte Reflexivität von blankem Meereis nahe der Eiskante das System im Wassergürtelzustand, wobei die durchschnittliche Eiskante bei einem Breitengrad von etwa $\pm 15^\circ$ liegt. Dieser stabile Wassergürtelzustand in ExoCAM tritt bei atmosphärischen CO_2-Konzentrationen zwischen 45 und 8000 ppmv auf. Der Übergang von einem gemäßigten, eisfreien Zustand beginnt bei 1400 ppmv CO_2, was die geologische Plausibilität des Wassergürtelzustands in ExoCAM bestätigt.

Die Analyse von ExoCAM-Simulationen zeigt die Merkmale von Wassergürtelzuständen, einschließlich Niederschlag, Verdunstung, saisonaler Eisbedeckung, den Einfluss von Wolken auf die einfallende Sonnenstrahlung und die Energiebilanz an der Oberkante der Atmosphäre. Darüber hinaus enthält diese Arbeit eine umfassende Installationsanleitung für ExoCAM auf Hochleistungscomputersystemen.

Contents

1 Introduction

For my Master's project, I investigate the climate dynamics of a Snowball Earth, specifically exploring the existence and geological plausibility of waterbelt states, using the climate model ExoCAM. This study delves into the intricate mechanisms that could have allowed for habitable conditions during periods of extreme global glaciation, providing insights into ancient climate systems. By comparing simulation results from ExoCAM with those from established models like CAM and ICON, this research aims to elucidate the factors that enable or hinder the formation of stable waterbelt states.

In this thesis, chapter 1 provides a concise outline of the scientific context inspiring my research inquiries. Chapter 2 presents the research questions and goals of this study. Chapter 3 offers a practical guide for the installation process of the ExoCAM software. The methodologies employed are detailed in chapter 4. Chapter 5 showcases the results and examines the accessibility of the waterbelt state using this model. Finally, the findings and implications are discussed in chapter 6.

Snowball Earth and Waterbelt States: State of the Art

The term „Snowball Earth“ is used to describe a state of our planet where the oceans are globally frozen over. This is exemplified by the ice-edge latitude, where, in the contemporary climate, the ice-edge is situated at approximately 75-80°N in the Arctic and at around 60-70°S in the Antarctic (Rasmussen et al. 2022). In this present-day climate, glaciation on sea level occurs exclusively at the poles. Throughout glacial Snowball episodes, sea ice extends into tropical latitudes. Given the high reflectivity of ice and snow, globally frozen oceans can persist for an extended period of time (Pierrehumbert et al. 2011).

Earth's history - Geological Evidence

Major snowball events very likely occurred 3 times in Earth's history (Hoffman et al. 1998). Once during the Paleoproterozioc era around 2420 Mya (million years ago) and twice during the Neoproterozoic timeframe: the Sturtian at 720 Mya and the Marinoan at 635 Mya. These ages are marked by extreme carbon fluctuations and global glaciation after a billion-year absence (Hoffman et al. 2017). Following petrological evidence, these ice ages are backed by geological formations called drop stones, which were moved to the ocean by extending glaciers and stayed at marine ground after deglaciation (Kennedy

et al. 1998). Today, drop stones can be found covered by sedimentary deposits called cap carbonates, which hint at very high levels of oceanic and therefore atmospheric CO_2 at the time - reaching many 10,000s ppmv (parts per million by volume); today's value is 415 ppmv (measured in January 2022) (NOAA Earth System Research Laboratory 2024). By measurement of the magnetic field of the deposits, a map for Rodinia, the supercontinent of the Neoproterozoic time, was created and these geological discoveries can be traced back to the tropics, indicating a globally frozen planet (Pierrehumbert et al. 2011).

Bifurcation and Ice-Albedo Runaway Feedback

The development of a Snowball Earth event is accompanied by a series of state changes in the Earth's climate system. The results of an energy balance climate model (EBM), as depicted in figure 1a by Abbot et al. (2011), indicate the existence of two stable states with a constant ice edge latitude. One of these states is characterised by an ice edge latitude at the poles, while the other is characterised by an ice edge latitude at the equator. Starting from the temperate climate, a decrease in radiative forcing causes the ice edge to expand towards the equator until it reaches a critical point called bifurcation point. Exceeding this tipping point will lead to the system falling into the snowball state due to the ice-albedo runaway feedback. The ice-albedo feedback is a positive feedback loop that amplifies the process of ice formation in Earth's climate system. Due to the difference in albedo (reflectivity of a surface) of the ocean, ice and snow, generation of sea ice leads to enhanced reflectivity. When there is a notable difference in albedo between the ice and ocean surfaces, the ice-albedo feedback mechanism shows significant amplification, where even small ice formation perturbs the system, leading to the onset of the Snowball bifurcation.

The global glaciation results in deactivation of silicate weathering, the an-organic carbon cycle, allowing a large build-up of CO_2, which is needed for deglaciation. This process occurs via volcanic activity over a time span of millions of years, leading to the second bifurcation point and the system falling back into today's climate. Solely reverting to initial values will not be enough to reinstate today's climate. The theory of Snowball Earth explains the geology well, as cap carbonates found in southern China (presumably of Marinoan age) constitute evidence for high CO_2 concentrations, which are required for deglaciation and drop stones hinting at land-glaciers in the tropics (Hoffman et al. 2017).

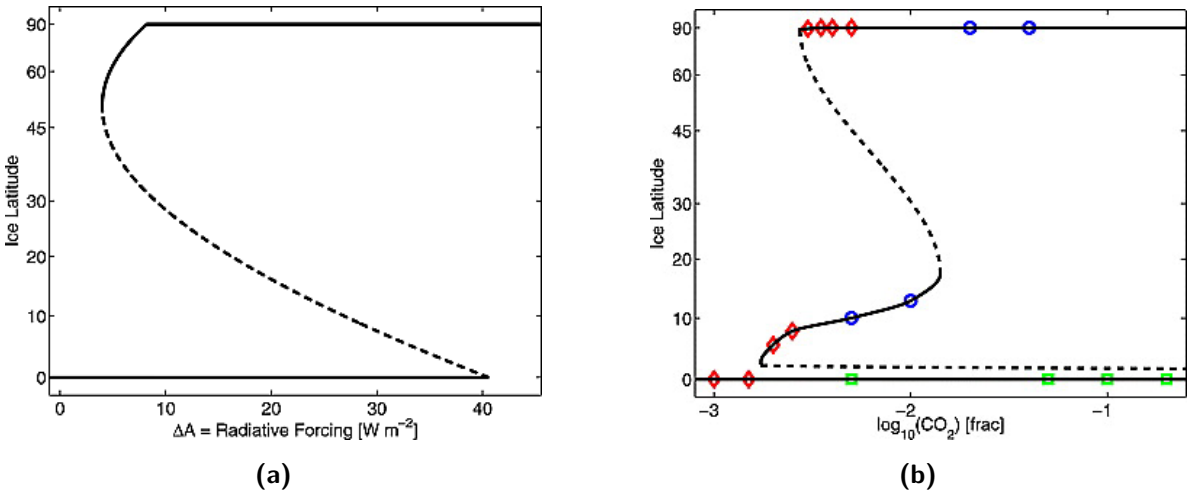

Figure 1 Bifurcation diagrams illustrating the absence and presence of the waterbelt state in subplots (a) and (b), respectively. The figures and caption have been adapted from Abbot et al. (2011).

Survival of life - Waterbelt State

As fossil discoveries of sponges showed evidence of advanced life from times before the Neoproterozoic (Maloof 2010), a few theories explaining life's preservation were suggested. These included black smokers creating warm oasis on ocean grounds or the thin ice theory (Pollard et al. 2005), yet this study focuses on the possibility of the waterbelt state.

Simulations by Abbot et al. (2011) in different climate models have shown the existence of this third stable state, the waterbelt state (figure 1b). An ice edge was found at about $\pm 10°$ latitude, which lasted over many hundred years. This waterbelt state is characterized by an open, ice-free ocean around the equator, which heavily supports the survival of life. A critical factor for reaching a waterbelt state is the difference in albedo for snow-free ice (0.45) and snow-covered ice (0.78) in the (sub-)tropics. If sea ice is snow-free, it can stop the ice-albedo runaway feedback and allow a stable ice edge at 10° (Abbot et al. 2011). In subtropical regions, the subsidence of the Hadley circulation leads to reduced precipitation and increased evaporation over high-albedo snow-covered sea ice. As a result, subtropical sea ice remains snow-free and relatively dark in appearance, reducing the strength of the ice-albedo feedback mechanism as sea ice migrates into these regions. This weakening of the ice-albedo feedback is significant enough to prevent a runaway effect and ultimately stabilise the climate in a waterbelt state (with the ice

edge remaining in close proximity to the equator), rather than progressing to a hard snowball scenario (Braun et al. 2022).

The top-of-atmosphere (TOA) albedo is influenced not only by the reflective properties of the surface but also by reflective substances present in the atmosphere, particularly clouds. The planetary albedo over ice-free ocean surfaces is primarily influenced by the reflection of shortwave radiation due to clouds. A higher planetary albedo enables the extension of waterbelt states toward lower latitudes by weakening the ice–albedo feedback as the planetary albedo increases. A significant contribution to planetary albedo by high clouds helps maintain stable waterbelt states by reducing the shortwave effects of variations in ice cover. When clouds are abundant and contribute to a high albedo over ice-free oceans, the waterbelt regime extends widely and is readily accessible. Conversely, when clouds are scarce, the waterbelt regime narrows and may become less accessible (Braun et al. 2022).

The hydrological cycle converts sea water and ice into water vapor, yet in Snowball Earth conditions characterized by low temperatures, evaporation, and consequently cloud formation, is restricted. The relative impact of precipitation and evaporation, denoted as P-E, can be investigated via figure 2. Figure 2a by Pierrehumbert et al. (2011) shows an annual mean precipitation minus evaporation (P-E) pattern depicting a typical Snowball state. It originates from the Fast Ocean Atmosphere Model v1.5 (FOAM) computed at a concentration of 2000 ppmv CO_2. At the equator, evaporation is higher than precipitation, indicating a zone of net ablation and water is transported toward the poles. This pattern contrasts sharply with the characteristic climate regimes found under modern conditions, or any that prevail in climates where the tropics remain free of glaciation (Pierrehumbert et al. 2011). On the contrary, figure 2b depicts the P-E plot from an ice-free and a waterbelt state with 5000 ppmv CO_2 found by Abbot et al. (2011). In the snowball state, P-E is about two orders of magnitude smaller than in other climatic states. The magnitude of P-E is directly related to the vertical mean of the convergence of the product of atmospheric meridional velocity and specific humidity.
In the waterbelt state, the spatial distribution of the P-E pattern plays a critical role in maintaining the state: regions with annual mean P-E above zero experience snow accumulation on sea ice, whereas regions with annual mean P-E below zero have bare sea ice surfaces with no snow cover for most of the year. As the tropical maximum in P-E, represented by the Inter-Tropical Convergence Zone (ITCZ), lies within the domain of the waterbelt state, sea ice located equatorward of about 20° remains predominantly

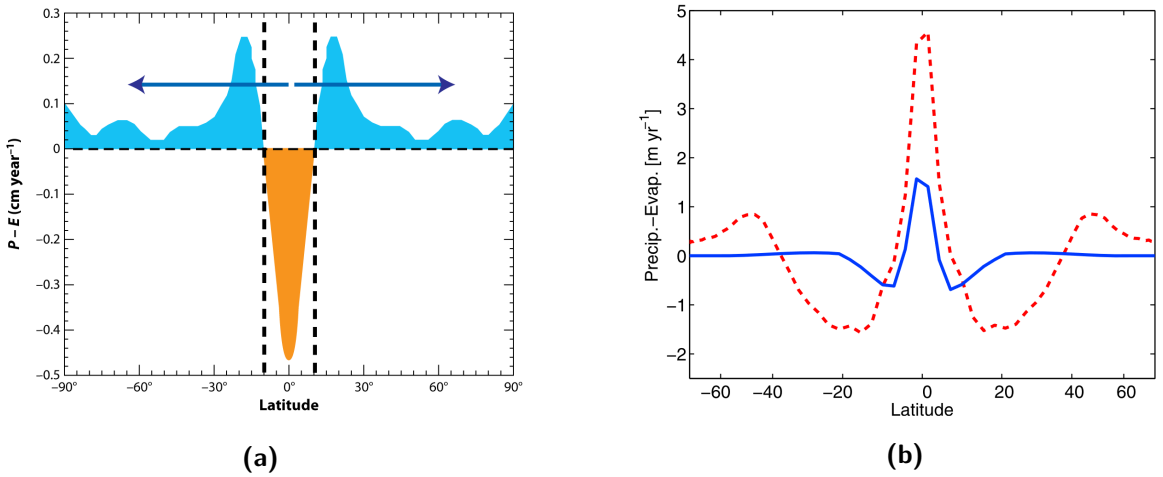

Figure 2 Annual and zonal mean precipitation minus evaporation for a Snowball state (subplot a), ice-free state (subplot b, red dashed) and Jormungand state (subplot b, blue). The subplots and their captions have been adapted from Pierrehumbert et al. (2011) and Abbot et al. (2011), respectively.

bare, and therefore darker than snow-covered sea ice, in this state. Although low-level cloud formation can still be present in the area of decent of the Hadley circulation, as described by Braun et al. (2022), one would expect clouds to be predominantly sparse and top-of-atmosphere albedo defined by surface albedo. With a sufficiently low albedo of the bare sea ice, the diminished ice-albedo feedback allows an ice-edge to be stable in the tropics near the equator (Abbot et al. 2011).

The Jormungand state

Within the definition of the waterbelt state, the Jormungand state, introduced by Abbot et al. (2011), serves as a subcategory to it. While the Jormungand state shares most characteristics of the waterbelt state, it is defined by a distinct area of bare sea ice cover near the ice edge, which heavily attenuates the ice-albedo runaway feedback. Given its defining feature of a narrow strip of open ocean encircling the planet, oscillating across the equator in response to seasonal variations, its name was inspired from Norse mythology, specifically referencing the world serpent, adversary of Thor. Figure 3 by Abbot et al. (2011) shows the seasonal variation of the ice-free ocean strip around the equator as a Hovmöller diagram simulated with an atmospheric CO_2 concentration of 2000 ppmv (Abbot et al. 2011). The open ocean is plotted in blue and regions of 100% ice coverage are plotted in white. The Jormungand state is named for the serpent-like

weaving of the narrow open ocean region in this diagram.

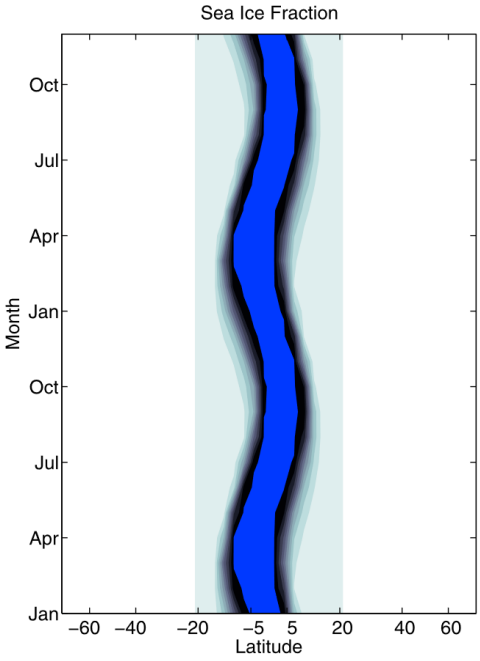

Figure 3 Hovmöller diagram of the zonal mean sea ice fraction in the Jormungand state. The figure and caption have been adapted from Abbot et al. (2011).

Bifurcation diagram and bifurcation points

The bifurcation diagram serves as a critical graphical representation, capturing the system's state and facilitating the comparison of different simulations. Figure 4 shows a conceptual bifurcation diagram, were the ice edge latitude, depicted on the y-axis, is plotted against a parameter representing radiative forcing, typically the atmospheric CO_2 concentration, on the x-axis. Three bifurcation points characterize the features of a waterbelt state: the lower bifurcation point (blue), the upper bifurcation point (yellow), and the bifurcation point transitioning from the ice-free (temperate) state (green).
When beginning the simulation in the waterbelt state, the lower bifurcation point signifies a CO_2 concentration threshold. Below this threshold, any reduction in climate forcing (specifically CO_2) causes the state to become unstable, resulting in a rapid transition to a hard snowball Earth within a relatively short simulated time span. Similarly, the upper bifurcation point represents another CO_2 concentration threshold. Beyond this threshold, any increase in climate forcing destabilizes the state, leading to a transition to a temperate state. Together, these points delineate the range of a stable waterbelt state.

In realistic terms, achieving the waterbelt state in simulations typically requires starting from the temperate, ice-free state. Starting from the state of hard snowball Earth necessitates a substantial increase in atmospheric CO_2 for deglaciation, surpassing the upper bifurcation point. Consequently, this skips the waterbelt state, causing the ice edge latitude to directly advance towards the poles. The third critical CO_2 concentration threshold, marking the bifurcation point from the ice-free (temperate) state, plays a pivotal role in describing the geological accessibility of the waterbelt state. Starting from the ice-free state, CO_2 concentrations below this threshold destabilize the state, leading to a transition to the waterbelt state. Conversely, if this CO_2 concentration falls below the lower bifurcation point, the transition from the ice-free state bypasses the waterbelt state and progresses directly to a hard snowball Earth. This situation confines the waterbelt state to climate simulations, as geologically, reaching the waterbelt state would be unfeasible.

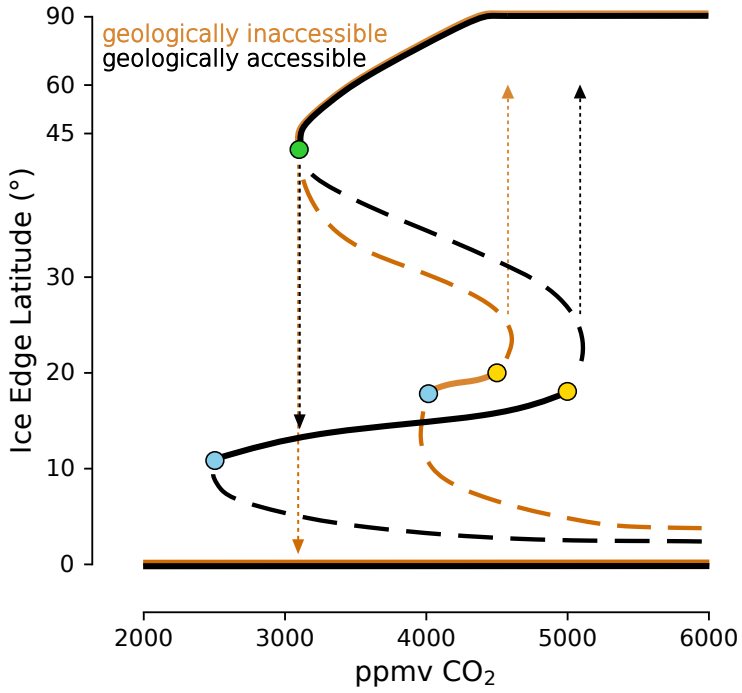

Figure 4 Conceptual bifurcation diagram, showcasing the geological accessibility of the waterbelt state. The data points are manually chosen and do not represent actual simulations. Blue dots represent lower bifurcation points, yellow dots represent upper bifurcation points and the green dot represents the bifurcation point from the ice-free state. Solid and dashed lines refer to stable and unstable states, respectively.

Waterbelt states in CAM and ICON

Figure 5 and its subplots (a), (b) and (c) show bifurcation diagrams of global-mean ice edge versus atmospheric CO_2 concentrations for previous studies using the climate models CAM, ICON and ICON WBF, respectively.

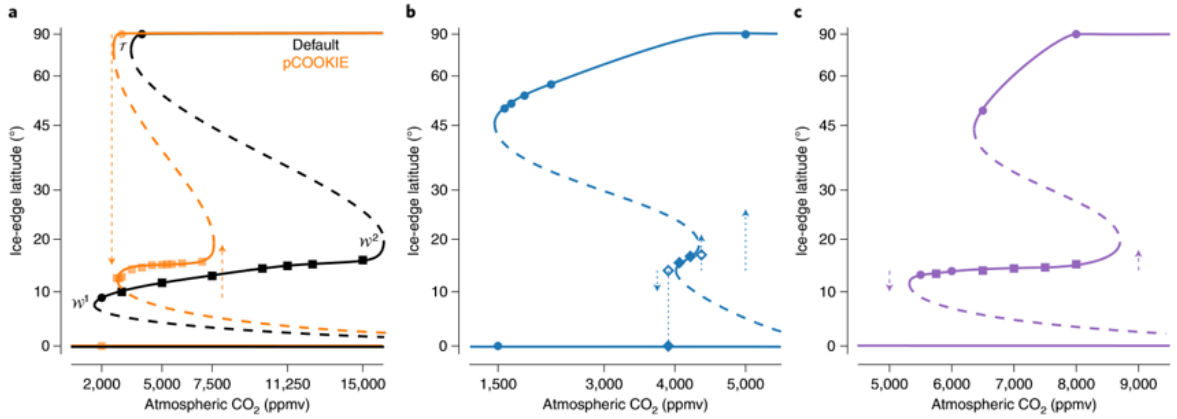

Figure 5 Bifurcation diagrams indicating the existence and absence of waterbelt states in the GCMs CAM and ICON. Subplot (a), (b) and (c) show results from climate models CAM, ICON and ICON WBF, respectively. The figure and caption have been adapted from Braun et al. (2022).

The Community Atmosphere Model (CAM) exhibits three distinct and stable climate regimes (Figure 5a). The first is a temperate regime, characterised by the absence or minimal extent of ice cover. The second is a waterbelt regime, which is defined by an ice edge situated between 9° and 15° latitude and the third is a snowball regime, which is characterised by global ice cover. The three relevant bifurcation points are found at distinct CO_2 levels: the temperate climate transition into the waterbelt state is found at 3000 ppmv CO_2, marking the bifurcation point from the ice-free state. The transition from waterbelt state to snowball climate occurs at 1750 ppmv CO_2, marking the lower bifurcation point and the transition from waterbelt state to the ice-free temperate climate is located at 15,000 ppmv CO_2, marking the upper bifurcation point. The waterbelt regime exists over a range of 13,000 ppmv and is therefore easily accessible from the temperate state. In comparison, results from ICON (Figure 5b) show a different scenario, where the waterbelt state is not geologically accessible from the temperate, ice-free state. Since the bifurcation point from the ice-free state is found at a lower CO_2 concentration of 1594 ppmv CO_2 then the lower bifurcation point at 4000 ppmv CO_2, identification of the waterbelt state in ICON simulations is increasingly difficult. To achieve the

results depicted in Figure 5c, a modification to the Wegener-Bergeron-Findeisen process (WBF) (Storelvmo et al. 2015) was applied to ICON by Braun et al. (2022), in order to weaken the WBF, which increases cloud liquid. Consequently, elevated atmospheric CO_2 concentrations are necessary to sustain a temperate climate, which brings the outcomes closer to those of CAM, seen in Figure 5a, as the bifurcation point from the temperate state rises to 6250 ppmv CO_2. The reduction in the liquid-to-ice conversion achieved through the WBF enables ICON to manifest waterbelt states that are accessible, as the results demonstrate a lower bifurcation point at 5250 ppmv CO_2 and an upper bifurcation point at 8500 ppmv CO_2 (Braun et al. 2022).

2 Research Question

To qualify as a plausible scenario of the cryogenic climate system, the waterbelt state must be replicable in various climate models. The primary objective of my master's thesis is to assess the existence and accessibility of the waterbelt state within the climate model ExoCAM. This will enable the possibility of expanding the list of climate models with a waterbelt state, which is not only physically accessible but also extends over a wide region of CO_2.

ExoCAM

ExoCAM (Wolf et al. 2022) is an exoplanet branch of the Community Earth System Model (CESM) version 1.2.1 (Vertenstein 2013). The model was designed for climate systems different from Earth in order to study extrasolar planets, which proved difficult when using common climate models. This was due to the constraint of free parameters to modern Earth's settings within cloud and convection routines, which manifested as a source of uncertainty in evaluating exoplanet climates. We choose the model parameters to represent those of Earth from approximately 500 million years ago, a period likely to have experienced a Snowball Earth event. We also employ idealizations in ocean dynamics and continental effects to simplify simulations. This also ensures optimal comparability with the results from Hörner (2023), which were obtained with the same settings using the climate model ICON (Icosahedral Nonhydrostatic Weather and Climate Model) (Giorgetta 2018), in order to assess the differences of clouds and ice properties between the models.

To reach the main goal of expanding the list of climate models with a physically accessible waterbelt state, I address the following research question:

How accessible is the waterbelt state in ExoCAM in comparison to CAM and ICON and how geologically plausible is it?

The motivation behind utilising a model such as ExoCAM is to ascertain whether the waterbelt state can also be identified in other models than ICON and Community Atmosphere Model (CAM). Furthermore, this approach paves the way for future utilisation

when investigating climates of extrasolar planets and their habitability. ExoCAMs improved radiation scheme and modification of cloud particle sizes in cloud microphysics in comparison to common 3D climate models may impact the ice-albedo runaway feedback and subsequently the representation of geologically plausible waterbelt states. The objective is to ascertain the extent of models that can simulate a geologically plausible waterbelt state and to conduct a direct comparison with the results from Braun et al. (2022) and Hörner (2023) with the climate models CAM and ICON. Given that ExoCAM is based on CAM, which simulates a greater number of clouds and generates a more geologically plausible waterbelt state than ICON (Braun et al. 2022), it can be expected that the results will indicate a waterbelt state with a wider and more accessible range of CO_2 concentration or radiative forcing.

3 ExoCAM on VSC4

This chapter describes the installation process of CESM 1.2.1 and the subsequent configuration of the ExoCAM package, including the radiative model ExoRT, on the high-performance-computing (HPC) system Vienna Scientific Cluster 4 (VSC4). This procedure involves acquiring the model, adjusting boundary conditions and executing the simulation.

ExoCAM and its building process as described by Wolf et al. (2022) consists of 3 installation parts:

1. CESM1.2 (the climate model ExoCAM is built on)
2. ExoCAM ("plugin" for CESM1.2 that allows the simulation of exoplanetary atmospheres)
3. ExoRT (new radiative model for exoplanets, it's separated from ExoCAM only because it's sometimes run as a standalone model)

3.1 Installing CESM 1.2.1

The installation process of CESM version 1.2.1 is described as a summary, following the official guide[1]:

Downloading CESM 1.2.1

CESM2 releases are publicly available on GitHub.[2] Using previous versions requires a registration[3] grating access to CESM version 1 (Login: guestuser; password: friendly).

After connecting to your HPC system via secure shell protocol (ssh), issue the following command to check out CESM 1.2.1 from the central source repository into a local sandbox directory:

[1] CESM Software Engineering Group (CSEG) NCAR. "CESM User's Guide (CESM1.2 Release Series User's Guide)" NCAR Community Earth System Model, 23.01.2023, `https://www2.cesm.ucar.edu/models/cesm1.2/cesm/doc/usersguide/book1.html`

[2] University Corporation for Atmospheric Research. "Models" NCAR Community Earth System Model, 23 Jan. 2023, `https://www.cesm.ucar.edu/models`

[3] `https://www2.cesm.ucar.edu/models/register/`

```
# List available CESM versions
>> svn list https://svn-ccsm-release.cgd.ucar.edu/model_versions
# Check out desired model version
>> svn co https://svn-ccsm-models.cgd.ucar.edu/cesm1/release_tags/
↪  cesm1_2_1 cesm1_2_1
```

This command establishes a directory a directory called `cesm1_2_1` that can be used to modify, build, and run the model.

Loading modules

To continue with the next steps, certain modules are needed. These can be loaded using either of the following commands, depending on your HPC system:

```
>> module load <package_name>
>> spack load <package_name>   # Load modules using HPC package manager
↪  spack
>> spack load /<HASH>          # Load modules using a known hash of a
↪  package

>> spack find                  # List available modules
>> spack find --loaded         # List loaded modules
```

To simplify this step and avoid complications, create a spack-environment, which loads multiple modules at once:

```
# Create a local environment
>> spack env create -d /path/to/envname
# Activate environment
>> spack env activate -p /path/to/envname

# Add and install packages (order matters):
>> spack add netcdf-fortran@4.6.0%oneapi@2022.2.1
>> spack install
>> spack add intel-oneapi-compilers@2022.2.1
>> spack install
>> spack add intel-oneapi-mpi@2021.7.1%intel@2021.7.1
>> spack install

>> spack env activate -p /path/to/envname   # Activate environment
>> despacktivate                            # Deactivate environment
```

Perl fixes on VSC4

VSC4 is missing a few essential perl libraries. They can be obtained via the publicly visible climate science branch (run by working group Voigt) of the Department of Me-

teorology and Geophysics on GitLab[4] and should be copied to the main installation directory `cesm1_2_1`. To automatically load the missing perl libraries on start-up, add the following line to the automatically executing configuration file `.bashrc`:

```
export PERL5LIB=~/cesm1_2_1/vsc4_fixes/perl5/lib/perl5:$PERL5LIB
```

To avoid future issues, navigate to the following file and edit line 448 to add a pair of parentheses:

```
# Edit file using VIM-editor
>> vi $HOME/cesm1_2_1/scripts/ccsm_utils/Case.template/ConfigCase.pm
...
foreach my $model (qw(COMP_ATM COMP_LND COMP_ICE COMP_OCN COMP_GLC
↪  COMP_ROF COMP_WAV)) {
...
```

Similarly to the previous task, navigate to the following file and edit line 1180 to escape the curved bracket ({) by inserting a backslash in front (\).

```
>> vi $HOME/cesm1_2_1/scripts/ccsm_utils/Case.template/ConfigCase.pm
...
if($text =~/^(.*)\$ENV\{(.*)}(.*)$/){
...
```

Creating a new case with a userdefined machine

As of January 2024, CESM1.2.1 recognizes 24 HPC systems.[5] To create a new case using an initially unsupported machine, the argument `-mach userdefined` can be used:

```
# Navigate to sub-directory "scripts"
>> cd cesm1_2_1/scripts/
# Create a new CESM case directory
>> ./create_newcase -case <case_name> -res f45_g37 -compset X -mach
↪  userdefined
...
Successfully created the case for userdefined
```

[4] Perl library fix.https://gitlab.phaidra.org/climate/cesm-on-vsc/-/tree/main/vsc5_fixes
[5] https://www2.cesm.ucar.edu/models/cesm1.2/cesm/doc/modelnl/machines.html

cesm_setup and xml variables

Navigate to the newly created case for set-up.

```
>> cd <case_name>/          # Navigate to case directory
>> ./cesm_setup             # Issue cesm_setup
```

If Perl issues occur, same as before, navigate to the troubling file (in this case: syntax error at `$HOME/cesm1_2_1/scripts/<case_name>/cesm_setup` line 252) and add a pair of parentheses:

```
>> vi cesm_setup
...
foreach my $model (qw(COMP_ATM COMP_LND COMP_ICE COMP_OCN COMP_GLC
↪  COMP_ROF COMP_WAV)) {
...
```

The output from running `cesm_setup` will indicate which xml variables are required to set. The definition of each xml-variable is documented at the NCAR CESM website.[6]

```
ERROR: must set xml variable OS to generate Macros file
ERROR: must set xml variable MAX_TASKS_PER_NODE to build the model
ERROR: must set xml variable MPILIB to build the model
ERROR: must set xml variable RUNDIR to build the model
ERROR: must set xml variable DIN_LOC_ROOT to build the model
ERROR: must set xml variable COMPILER to build the model
ERROR: must set xml variable EXEROOT to build the model
Correct above and issue cesm_setup again
```

Modifications in xml-variables should always be executed via the `./xmlchange`-command which supports error checking as part of the implementation and minimizes the chance of typographical errors.[7]

```
# How to use xmlchange to change values of variables
>> cd $HOME/cesm1_2_1/scripts/<case_name>
>> ./xmlchange var=value,var2=value2

# Operating system - Do not edit unless for userdefined machine
>> ./xmlchange OS=LINUX
```

[6] University Corporation for Atmospheric Research. "CESM1.2 MODEL COMPONENT NAMELISTS" NCAR Community Earth System Model, 23.01.2023,https://www2.cesm.ucar.edu/models/cesm1.2/cesm/doc/modelnl/

[7] cf. CESM Software Engineering Group (CSEG) NCAR. "CESM User's Guide (CESM1.2 Release Series User's Guide)" NCAR Community Earth System Model, 23.01.2023,https://www2.cesm.ucar.edu/models/cesm1.2/cesm/doc/usersguide/x1968.html

```
# Change EXEROOT in env_build.xml
>> ./xmlchange EXEROOT=/home/fs71767/awaba/cesm1_2_1/scripts/test1/bld
# Change COMPILER in env_build.xml
>> ./xmlchange COMPILER=intel
# Change MPILIB in env_build.xml
>> ./xmlchange MPILIB=openmpi
# Change MAX_TASKS_PER_NODE
>> ./xmlchange MAX_TASKS_PER_NODE=48
# Change path to your $DATA directory
>> cd $DATA
>> pwd
/gpfs/data/fs71767/awaba
>> ./xmlchange RUNDIR=/gpfs/data/fs71767/awaba/cesm/$CASE/run
# Change DIN_LOC_ROOT in env_run.xml
>> ./xmlchange DIN_LOC_ROOT=/gpfs/data/fs71767/awaba/inputdata
```

Running `./cesm_setup` again, will now create a Macros and build files, but once again Perl fixes are needed. Navigate to the troubling file (in this case: syntax error at `$HOME/cesm1_2_1/models/drv/bld/build-namelist` line 781) and add a pair of parentheses:

```
>> vi $HOME/cesm1_2_1/models/drv/bld/build-namelist
...
foreach my $model (qw(cpl atm lnd ice ocn glc rof wav)) {
...
```

Running `./cesm_setup` again will now successfully set-up the case.

Macros file

Edit the newly created Macros file inside the case directory to add the path to the netcdf-installation of your HPC-system. This could either be a fixed path or an environment variable configured in `/<case_name>/env_mach_specfic` or via modules. You may also need to adjust additional macro variables like `MPI_PATH`, based on your specific system configuration.

```
>> whereis filename -l          # Find desired installation path
```

Originally:

```
>> vi Macros
SLIBS+=# USERDEFINED $(shell $(NETCDF_PATH)/bin/nc-config --flibs)
...
NETCDF_PATH := USERDEFINED_MUST_EDIT_THIS
```

Change to:

```
SLIBS+= -L$(NETCDF_DIR) -lnetcdff -Wl,--as-needed,-L$(NETCDF_DIR)/lib
↪  -lnetcdff -lnetcdf $(MKL)
...
NETCDF_PATH:=/gpfs/opt/sw/skylake/spack-0.19.0/opt/spack/
↪  linux-almalinux8-skylake_avx512/intel-2021.7.1/
netcdf-fortran-4.6.0-24vcften2kl7ljr2vyny7guxrtn4z7kk/
```

Building the case

This step is prone to failure if paths to compilers, compiler versions, or libraries are incorrectly configured, if compiler options are not properly defined, or if machine-specific environment variables are not correctly set.[8] Also remember to activate the previously created spack environment to load modules.

```
>> ./<case_name>.build
...
ERROR: buildlib.mct failed, see
↪  $HOME/cesm1_2_1/scripts/test1/bld/mct/mct.bldlog.230605-171608
ERROR: cat $HOME/cesm1_2_1/scripts/test1/bld/mct/mct.bldlog.230605-171608
```

Multiple error fixes are needed to solve this issue:

a. Change compiler variables in `$HOME/cesm1_2_1/scripts/ccsm_utils/Machines/config_compilers.xml`

from:

```
<compiler COMPILER="intel">
...
<MPIFC> mpif90 </MPIFC>
<MPICC> mpicc  </MPICC>
</compiler>
```

to:

```
<MPIFC> mpiifort </MPIFC>
<MPICC> mpiicc  </MPICC>
```

[8] CESM Software Engineering Group (CSEG) NCAR. "CESM User's Guide (CESM1.2 Release Series User's Guide)" NCAR Community Earth System Model, 23.01.2023,https://www2.cesm.ucar.edu/models/cesm1.2/cesm/doc/usersguide/x1748.html

b. Change compiler variables in `$HOME/cesm1_2_1/scripts/<case_name>/Macros`

from:

```
MPIFC:= mpif90
MPICC:= mpicc
SCC:= icc
```

to:

```
MPIFC:= mpifort
MPICC:= mpiicc
SCC:= icx
```

c. Missing pio directory fix

Because the link to pio is broken in `cesm1_2_1/SVN_EXTERNAL_DIRECTORIES` (which only gets used at the very start of the cesm-installation), we have to download it manually.
Download the `pio1_7_2` source code from GitHub,[9] extract the content (using a file archiver software like winrar, 7zip, etc.) and upload the new pio directory with to following path `/cesm1_2_1/models/utils/pio/`. Adjust permissions of the `configure` file within this directory:

```
>> cd /cesm1_2_1/models/utils/pio/
>> chmod 777 configure
```

Download the missing genf90.pl file manually from the ParallelIO-GitHub[10] and upload with the following path: `/$HOME/cesm1_2_1/tools/cprnc/genf90/genf90.pl`

Issuing the build command inside the case directory is now successful.

```
>> ./<case_name>.build
...
CESM BUILDEXE SCRIPT HAS FINISHED SUCCESSFULLY
```

[9] Edwards, Jim. "pio1_7_2", GitHub, 23 Jan. 2023, https://github.com/NCAR/ParallelIO/releases/tag/pio1_7_2

[10] Edwards, Jim. "genf90_140121", GitHub, 23 Jan. 2023, https://github.com/PARALLELIO/genf90/releases/tag/genf90_140121

Running the case

To configure the local batch environment and the job launch command, adjustments to `<case_name>.run` are required. Add `SBATCH` commands at the top of `<case_name>.run` (adjust to your personal paths and e-mail address) and edit the `job launching` section in `<case_name>.run` (un-comment either `mpiexec` or `mpirun`) and adjust the value of the attribute `-n` depending on your HPC systems properties.

```
    >> cd cesm1_2_1/scripts/<case\_name>
    >> vi <case\_name>.run
    ...
    #SBATCH --account=p71767
    #SBATCH --partition=skylake_0096
    #SBATCH --qos=skylake_0096_devel
    #SBATCH --job-name=test1
    #SBATCH --nodes=1
    #SBATCH --ntasks-per-node=48
    #SBATCH --ntasks-per-core=1
    #SBATCH --output=/home/fs71767/awaba/logfiles/LOG.<case_name>.%j.o
    #SBATCH --error=/home/fs71767/awaba/logfiles/LOG.<case_name>.%j.o
    #SBATCH --exclusive
    #SBATCH --time=00:10:00
    #SBATCH --mail-user=<your_email@adress>
    #SBATCH --mail-type=BEGIN,END,FAIL
    ...
#==================================================================
# USERDEFINED
# edit job launching
#==================================================================
mpiexec -n 48 $EXEROOT/cesm.exe >&! cesm.log.$LID
#mpirun -np 48 $EXEROOT/cesm.exe >&! cesm.log.$LID

wait
echo "`date` -- CSM EXECUTION HAS FINISHED"
```

Finally, `sbatch <case_name>.run` is the job submission of the run script.

Defining VSC4 as a known machine

An initially unknown machine (HPC system) can be configured as a known machine. Create the following section in `cesm1_2_1/scripts/ccsm_utils/Machines/config_machines.xml` and adapt for your personal path:

```
<machine MACH="vsc4">
    <DESC>VSC4, os is Linux, 48 pes/node, batch system is SLURM</DESC>
```

```
    <OS>LINUX</OS>
    <COMPILERS>intel</COMPILERS>
    <MPILIBS>openmpi,mpich,mpt,mpt,ibm,mpi-serial</MPILIBS>
    <RUNDIR>/gpfs/data/fs71767/awaba/cesm/$CASE/run</RUNDIR>
    <EXEROOT>/gpfs/data/fs71767/awaba/cesm/$CASE/bld</EXEROOT>
    <DIN_LOC_ROOT>$DATA/inputdata</DIN_LOC_ROOT>
    <DIN_LOC_ROOT_CLMFORC>$ENV{CESMROOT}/lmwg</DIN_LOC_ROOT_CLMFORC>
    <DOUT_S_ROOT>/home/fs71767/awaba/archive/$CASE</DOUT_S_ROOT>
    <DOUT_L_MSROOT>csm/$CASE</DOUT_L_MSROOT>
    <CCSM_BASELINE>$ENV{CESMDATAROOT}/ccsm_baselines</CCSM_BASELINE>
    <CCSM_CPRNC>$ENV{CESMDATAROOT}/tools/cprnc/cprnc</CCSM_CPRNC>
    <BATCHQUERY>bjobs -w</BATCHQUERY>
    <BATCHSUBMIT>bsub &lt;</BATCHSUBMIT>
    <SUPPORTED_BY>cseg</SUPPORTED_BY>
    <GMAKE_J>8</GMAKE_J>
    <MAX_TASKS_PER_NODE>30</MAX_TASKS_PER_NODE>
    <PES_PER_NODE>48</PES_PER_NODE>
</machine>
```

Create the following section in `cesm1_2_1/scripts/ccsm_utils/Machines/config_compilers.xml`:

```
<compiler MACH="vsc4">
    <NETCDF_PATH> /gpfs/opt/sw/skylake/spack-0.19.0/opt/spack/
    ↪  linux-almalinux8-skylake_avx512/intel-2021.7.1/
    ↪  netcdf-fortran-4.6.0-24vcften2kl7ljr2vyny7guxrtn4z7kk/ </NETCDF_PATH>
    <PNETCDF_PATH></PNETCDF_PATH>
    <ADD_SLIBS>$(shell $(NETCDF_PATH)/bin/nc-config --flibs)</ADD_SLIBS>
    <ADD_CPPDEFS></ADD_CPPDEFS>
    <CONFIG_ARGS></CONFIG_ARGS>cesm1_2_1/scripts/ccsm_utils/
    ↪  Machines/mkbatch.userdefined
    <ESMF_LIBDIR></ESMF_LIBDIR>
    <MPI_LIB_NAME></MPI_LIB_NAME>
    <MPI_PATH></MPI_PATH>
</compiler>
```

Within the directory `cesm1_2_1/scripts/ccsm_utils/Machines/`, create `mkbatch.vsc4` by copying and renaming an existing machine.

Now the argument `-mach vsc4` can be used to create a new case on the known machine VSC4:

```
    >> ./create_newcase -case CASENAME -res f45_g37 -compset X -mach vsc4
```

3.2 Installing ExoCAM and ExoRT

The installation process of ExoCAM is described as a summary, following the official guide.[11]

Downloading ExoCAM and ExoRT

First, checkout ExoCAM[12] and it's standalone radiative scheme ExoRT[13] packages from GitHub to the home directory:

```
>> cd
>> git clone https://github.com/storyofthewolf/ExoRT.git
>> git clone https://github.com/storyofthewolf/ExoCAM.git
```

Place the new system files from `../ExoCAM/cesm1.2.1/ccsm_utils_files` to the appropriate location within the CESM model. Place the following files in the directory `../cesm1_2_1/scripts/ccsm_utils/Machines`:

```
config_compilers.xml
config_machines.xml
env_mach_specific.hyak
env_mach_specific.summit
env_mach_specific.discover
mkbatch.hyak
mkbatch.summit
mkbatch.discover
```

Place the following file in directory
`../cesm1_2_1/scripts/ccsm_utils/Case.template`:

```
config_compilers.xml
```

Place the following file in directory
`../cesm1_2_1/models/atm/cam/bld/namelist_files`:

```
namelist_definition.xml
```

[11] Wolf, Eric. "ExoCAM/cesm1.2.1/instructions /general_instructions.txt" GitHub, 24.01.2023, https://github.com/storyofthewolf/ExoCAM/blob/main/cesm1.2.1/instructions/general_instructions.txt

[12] Wolf, Eric. "ExoCAM " GitHub, 24.01.2023, https://github.com/storyofthewolf/ExoCAM.git

[13] Wolf, Eric. "ExoRT " GitHub, 24.01.2023, https://github.com/storyofthewolf/ExoRT.git

Creating a new case with ExoCAM

ExoCAM comes with a varity of model options offering the choice between aqua and land planets, finite volume dynamical core ("fv") and spectral element dynamical core ("se"; on a cubed sphere grid) or the additional option for circumbinary (continents + slab ocean, finite volume dycore, cam4 phys) or experimental (developer) settings. These build configurations are described in the configs-README file[14] on GitHub in more detail and are chosen by using the corresponding resolution argument. For example, a new case using an aquaplanet model with the finite volume dynamical core, which is supported with a $4° \times 5°$ resolution, is created by heading to `../cesm1_2_1/scripts/` and issuing the following command:

```
>> ./create_newcase -case <case_name> -res f45_f45 -mach vsc4 -compset
↪  E2000C4AQI
```

The spectral element dynamical core can also be run on a higher resolution:

```
>> ./create_newcase -case <case_name> -res ne5np4_ne5np4 -mach vsc4
↪  -compset E2000C4AQI
>> ./create_newcase -case <case_name> -res ne16np4_ne16np4 -mach vsc4
↪  -compset E2000C4AQI
```

Alternatively to creating a new case, a clone of an old case can be created to preserve local modifications. The argument `-case` describes the name or path of the new case, `-clone` describes the full path of the case to be cloned.

```
>> ./create_clone -case <new_case> -clone <old_case>
```

Link ExoRT radiative transfer model and set configure options

To link ExoRT packages with ExoCAM, a radiative transfer version for 3D model hook up has to be chosen[15].

```
src.cam.n68equiv          !! September 2020, preferred version to use !!
src.cam.n84equiv          !! Identical to n68eqiuv except for extended
                          !! shortwave bins below 0.2 um; used for F-star
                          !! cases (10000 K > T > 6500 K) where UV radiation
                               !! below 0.2 um is significant
```

[14] Wolf, Eric. "ExoCAM/cesm1.2.1/configs/" GitHub, 24.01.2023, https://github.com/storyofthewolf/ExoCAM/tree/main/cesm1.2.1/configs

[15] Wolf, Eric. "ExoRT/3dmodels/" GitHub, 24.01.2023, https://github.com/storyofthewolf/ExoRT/tree/main/3dmodels

```
src.cam.n42h2o            !! Originated in Kopparapu et al. (2017) and related
↪  papers
src.cam.n68h2o            !! Used in Wolf et al. (2019)
src.cam.n28archean        !! Originated in Wolf & Toon (2013)
src.cam.n28archean.haze   !! Special modifcation to include hazes from
                          !! CESM-CARMA; also requires ExoCAM "carma"
                          ↪  additional
                          !! files.  Note that exo_radiation_cam_intr.F90 is
                          !! unqiue to this directory, containing native
                          ↪  CAM-CARMA
                          !! hook-ups.
```

To choose the recommended spectra, issue the following command with adjusted paths in your case directory:

```
>> cd $HOME/cesm1_2_1/scripts/<case_name>/
>> ./xmlchange CAM_CONFIG_OPTS="-nlev 40 -phys cam4 -usr_src
↪  $HOME/ExoRT/3dmodels/src.cam.n68equiv"
```

Radiative transfer models, ready for linking with CESM in 3D, are located at `../ExoRT/3dmodels`. The argument `-nlev` sets the number of vertical levels and `-phys` assigns the physics package. The default physics package `-phys cam4` utilizes the Rasch & Kristjansson "RK" cloud scheme. Interchangeably, the more advanced Morrison and Gettleman "MG" cloud scheme from cam5 is available by amending the `./xmlchange CAM_CONFIG_OPTS` command with `-chem none -microphys mg1` and by uncommenting the appropriate options in the `user_nl_cam` namelist file.[16]

Copy SourceMods and namelist files to case directory

The ExoRT package includes SourceMods and namelist files, which contain paths to the ExoCAM distribution that have to be adjusted accordingly.
Open the namelist files (`user_*`) and change the paths pointing to the initial files to match the location of the ExoCAM distribution. Also, open `SourceMods/src.share/exoplanet_mod.F90` and edit the path of `exo_solar_file` to match the ExoRT path. Edit or verify the correct path for `exort_rootdir` in the file `ExoRT/3dmodels/src.cam.n******/sys_rootdir.F90`. Optionally, if you wish to make modifications to the radiative transfer modules, copy the RT folder

[16] cf. Wolf, Eric. "ExoCAM/cesm1.2.1/instructions /general_instructions.txt" GitHub, 24.01.2023, https://github.com/storyofthewolf/ExoCAM/blob/main/cesm1.2.1/instructions/general_instructions.txt

`$EXORT_PATH/ExoRT/3dmodels/src.cam.n******` into your `$CASEROOT/SourceMods` directory, and change `-usr_src config opt` approriately.

Copy the `SourceMods` directory from `../ExoCAM/cesm1.2.1/configs/$model_config` and `namelist_files` from `../ExoCAM/cesm1.2.1/configs/$model_config/namelist_files/*` to your case directory (`$CASEROOT`) issuing the following commands[17]:

```
>> cd $HOME/cesm1_2_1/scripts/<case_name>/
>> cp -r $HOME/cesm1-exocam/ExoCAM/cesm1.2.1/configs/cam_aqua_fv/
↪  SourceMods .
>> cp /home/fs71767/awaba/cesm1-exocam/ExoCAM/cesm1.2.1/configs/
↪  cam_aqua_fv/namelist_files/* .
```

Alternatively, when using the spectral element dynamical core ("se"), issue the following commands:

```
>> cd $HOME/cesm1_2_1/scripts/<case_name>/
>> cp -r /home/fs71767/awaba/cesm1-exocam/ExoCAM/cesm1.2.1/configs/
↪  cam_aqua_se/SourceMods .
>> cp /home/fs71767/awaba/cesm1-exocam/ExoCAM/cesm1.2.1/configs/
↪  cam_aqua_se/namelist_files/ne16np4/* .
```

Building the case

If if the simulation will be computed on multiple nodes, `NTASKS_ATM` has to be changed using `xmlchange` before `cesm_setup` is issued. The value of `ntasks-per-node` has to be multiplied with the number of nodes available on your HPC system. For 7 nodes on VSC4, the following commands are issued:

```
>> cd $HOME/cesm1_2_1/scripts/<case_name>/
>> ./xmlchange NTASKS_ATM=336
>> ./cesm_setup
```

Changes in model setup (e.g. solar constant, obliquity, atmosphere content, ...) have to be taken within `$CASEROOT/SourceMods/src.share/exoplanet_mod.F90` before building. Albedo values can be changed within `$CASEROOT/user_nl_cice`. Within the `$CASEROOT` directory, issue the following command to build the case:

```
>> ./<case_name>.build
```

[17] cf. ibid.

Running the case

Change runtimes and resubmission settings within `$CASEROOT/env_run.xml`. E.g. to simulate 50 years by resubmitting after every 10th year, set `./xmlchange STOP_OPTION=nyears`, `./xmlchange STOP_N=10` and `./xmlchange RESUBMIT=4` ($10 + 10 \cdot 4 = 50$). A lower set time corresponds to a lower queue time. When resubmitting after 10 simulated years (`STOP_N=10`) utilizing 7 nodes on VSC4, a minimal wallclock of `time=06:00:00` is recommended. A description for all options available within `$CASEROOT/env_run.xml` is provided by NCAR.[18]

At the top of `$CASE.run` the batch submission is set. Adjust the directories for log-files and email address for reports accordingly:

```
#!/bin/csh -f
#=======================================================================
# VSC4
# This is where the batch submission is set.  The above code computes
# the total number of tasks, nodes, and other things that can be useful
# here.  Use PBS, BSUB, or whatever the local environment supports.
#=======================================================================

#SBATCH --account=p71767
#SBATCH --partition=skylake_0096
####SBATCH --qos=skylake_0096_devel
#SBATCH --nodes=7
#SBATCH --ntasks-per-node=48
#SBATCH --ntasks-per-core=1
#SBATCH --exclusive
#SBATCH --time=13:00:00
#SBATCH --output=$HOME/logfiles/LOG.<case_name>.%j.o
#SBATCH --error=$HOME/logfiles/LOG.<case_name>.%j.o
#SBATCH --mail-user=<your.email@address>
#SBATCH --mail-type=BEGIN,END,FAIL

#limit coredumpsize 1000000
#limit stacksize unlimited
```

Within `$CASEROOT` directory, issue the following command to run the model:

```
>> sbatch <case_name>.run        # Submit your run to the queue

>> squeue --user $USER           # Check ongoing sbatch submissions
>> scancel <JOBID>               # Cancel sbatch submissions
>> sqos                          # Check available HPC resources
```

[18] CESM Software Engineering Group (CSEG) NCAR. "env_run.xml variables" NCAR Community Earth System Model, 24 Jan. 2023, https://www2.cesm.ucar.edu/models/cesm1.2/cesm/doc/modelnl/env_run.html#run_stop

The status of an ongoing simulation can be found in `$CASEROOT/CaseStatus` or by consulting the logfile in `$CASEROOT/run/atm.log.*`. Outputs will be written to `$DATA/cesm/<case_name>/atm/hist/`.

Restarting a run - branch run

In a branch run, all components are initialized using a consistent set of restart files from a previous run (determined by the `$RUN_REFCASE` and `$RUN_REFDATE` variables in `env_run.xml`). To set up a branch run, locate the restart tar file or restart directory for `$RUN_REFCASE` and `$RUN_REFDATE` from a previous run, then place those files in the `$RUNDIR` directory of the new case:

```
>> cp -a $DATA/cesm/<old_case>/rest/0101-01-01-00000/.
↪  $DATA/cesm/<new_case>/run
```

Finally, within `env_run.xml`, set `$RUN_TYPE` to `branch`.

4 Methodology

For my master's project, I am using the ExoCAM (Wolf et al. 2022) and ExoRT plugin (a new radiative model for exoplanets) for CESM 1.2.1 (Vertenstein 2013) on the HPC system Vienna Scientific Cluster 4 (VSC4). As I want to compare ExoCAM's results with previously achieved results from other climate models, I am going to use the same settings used in those studies to ensure optimal comparability (Hörner 2022).

4.1 Model and simulation setup

To address my research questions and possibly expand the list of climate models with a physically accessible waterbelt state, I utilize the climate model ExoCAM (Wolf et al. 2022), an exoplanet branch of the Community Earth System Model (CESM) version 1.2.1 (Vertenstein 2013). The installation and subsequent simulations will be conducted on Vienna Scientific Cluster 4 (VSC4), which is Austria's most powerful high-performance computer. The system reaches a performance of 2.7 PFlop/s and is ranked 353 on the Top 500 list[19] of most powerful high-performance computer systems in 2024 and even reached rank 82 in 2019.[20]

ExoCAM, one of the core models studied in the TRAPPIST-1 Habitable Atmosphere Intercomparison (THAI) project, is designed to simulate the atmospheres of terrestrial extrasolar planets around various stars. ExoCAM features a unique radiative transfer package called ExoRT, which allows for flexible radiative transfer calculations necessary for a wide range of atmospheric compositions. ExoRT[21], a correlated-k radiative transfer package for 3-D climate models, was created as a separate 1D offline version of ExoCAM to simplify development, updates, and testing. ExoCAM provides support for a range of standard configurations, along with options to adjust planetary parameters and atmospheric compositions. Notably, ExoCAM supports several configurations, including aquaplanet, land-covered, and mixed land-ocean planets, and can be run at various resolutions and vertical layerings. The model has been instrumental in studying different exoplanet climates and evaluating the robustness of cloud and convection parameters. It is continually updated and accessible via GitHub[22], providing a comprehensive tool

[19] "TOP500 LIST - JUNE 2024", PROMETEUS Professor Meuer Technologieberatung, 14 June 2024, https://top500.org/lists/top500/list/2024/06/?page=4

[20] "VSC-4 – most powerful supercomputer in Austria", Vienna Scientific Cluster, 28 Apr. 2024, https://vsc.ac.at//systems/vsc-4/

[21] Wolf, Eric. "ExoRT ", GitHub, 08 Apr. 2024, https://github.com/storyofthewolf/ExoRT

[22] Wolf, Eric. "ExoCAM ", GitHub, 08 Apr. 2024, https://github.com/storyofthewolf/ExoCAM

for exoplanet climate modeling (Wolf et al. 2022).

Although ExoCAM is designed to support extraterrestrial interstellar objects with characteristics that deviate from those of Earth, the simulation settings in my study are set to represent an Earth-like planet. To ensure optimal comparability, the model setup is chosen to match the presets of former studies by Hörner (2023), utilizing the climate model ICON (Giorgetta 2018), as closely as possible. The simulation involves using an aqua-planet without continents, a slab ocean with a universal depth of 50 meters and a finite volume dynamical core. To simulate characteristics of an Earth-like planet at a time around 500 million years ago, where a Snowball-Earth event was actually feasible, an orbital period (solar year) of 360 days is applied. With a solar constant of 1285 Wm^{-2}, the weaker solar irradiation of the reference time (94% of its present value) is accounted for. The planets obliquity is set to 23.5°, an average of Earth's actual value, which has varied between 22.1 and 24.5 degrees with respect to Earth's orbital plane over the last million years as described by Milankovitch cycles (Laskar et al. 2004). For simplicity, an eccentricity of zero is applied, which corresponds to a circular orbit (Pierrehumbert et al. 2011). Albedo values for bare and snow-covered sea ice are set to 0.45 and 0.79 respectively, which were found for surface temperatures below -1°C by Abbot et al. (2011) using CAM. The atmosphere's well-mixed greenhouse gases only consist of nitrogen (N_2) and carbon-dioxide (CO_2), where N_2 has a fixed default partial pressure value of 0.999598 bar. Although ExoCAM supports higher resolutions when using a cubed sphere dynamical core and was successfully run at a resolution of up to 0.47°×0.63° (Komacek 2019), the vast majority of studies that use ExoCAM employ the default resolution of 4°×5° (Wolf et al. 2022) with a 40 layer vertical grid, spanning 3 orders of magnitude in pressure, which seems sufficient for this study and is therefore chosen.

4.2 Initial Conditions

Initial conditions of ExoCAM can be changed to account for a variety of configuration options (like land-ocean presets, cloud physics scheme, aerosol treatments or radiative transfer modules and spectra), but the default options prove to fit well for the purpose of waterbelt state analysis. At the first timestep, the simulated planet is completely free of ice. All grid cells have ice-fraction values of zero, so a theoretical ice-edge-latitude is calculated at ±90°.

Figure 6 shows the surface temperature for the default settings of initial conditions ranging between +28°C at the equator and −24°C at the poles. Values of high temperature are indicated in red, values of low temperature are represented by blue, while the freezing point (0°C) is represented by white shading. The freezing point can be found at a latitude of approximately 54° North/South. Naturally, the ice-edge-latitude will form at these values and monitoring will commence from this point onward.

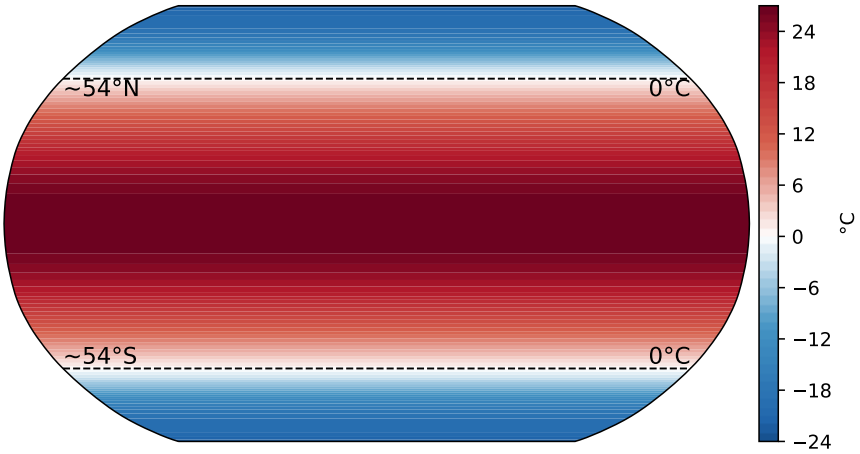

Figure 6 Global map of surface temperature values of the initial conditions.

Figure 7a and 7b present the zonal mean of the temperature values computed by the initial conditions in two-dimensional (2D) and three-dimensional (3D) space, respectively. Subfigure 7a represents the surface temperature as it is plotted against the latitude, in a line-plot. Subfigure 7b illustrates the variation of temperature across different latitudes and verticality, represented by atmospheric pressure, as a colormesh plot. The x-axis represents latitude, ranging from −90° to 90°, while the y-axis represents pressure, with values increasing from top to bottom. The color intensity at each point on the plot corresponds to the temperature, with warmer temperatures indicated by lighter shades and cooler temperatures by darker shades of green. The highest temperatures are noted at the surface of the equator, with a subsequent decrease in temperature as one moves vertically upwards and poleward.

4.3 Conversion between partial pressure and concentration

The radiative forcing of the simulated atmosphere in response to changes in climate is adjusted based on the concentration of greenhouse gases. As the simulated atmosphere

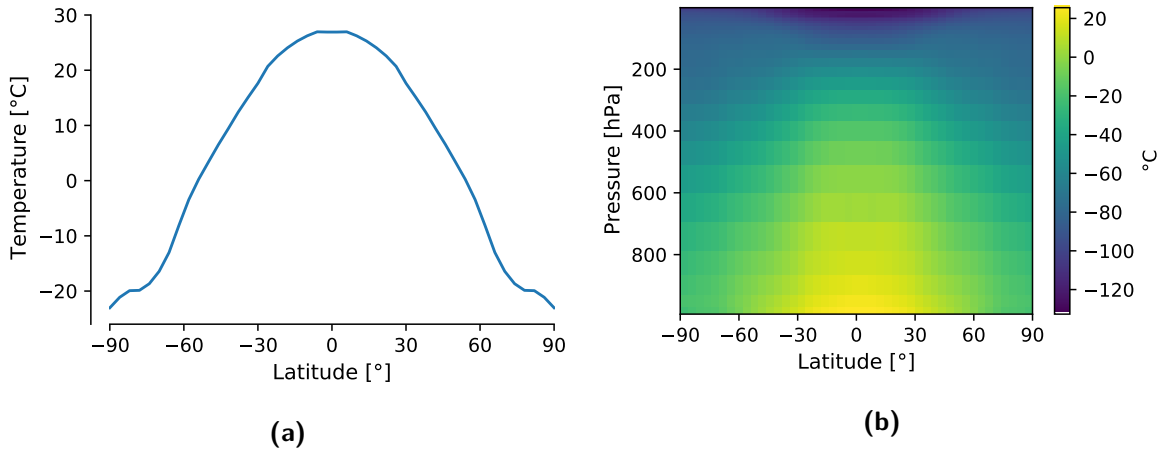

Figure 7 Zonal mean of initial condition temperature data using ExoCAM.

in ExoCAM's initial condition only contains nitrogen and carbon dioxide, CO_2 is the only variable subject to change. Atmospheric gas concentration is measured in bars of partial pressure. For the sake of clarity, concentration values are converted to parts per million by volume, henceforth will be referred to as ppmv. This unit expresses the concentration of one substance in a mixture relative to the volume of the entire mixture. For instance, if a gas mixture contains 1 ppmv of a certain pollutant, it means that one part of the pollutant gas is present for every million parts of the gas mixture (International Union of Pure and Applied Chemistry (IUPAC) 2007).

This paragraph explains the conversion from ppmv to partial pressure (bar), crucial for adjusting parameters in ExoCAM. As the conversion is not straightforward, it requires a clear and concise explanation. As described by Pierrehumbert et al. (2011), to determine the CO_2 inventory of the atmosphere, the pressure p_{I,CO_2} is introduced. This represents the surface pressure that the CO_2 in the atmosphere would have if it was the only component. If we refer to the inventory of dry background air (here N_2) as $p_{I,a}$, then the total surface pressure can be calculated as $p_{tot} = p_{I,CO_2} + p_{I,a}$. According to Dalton's law, if χ represents the molar concentration of carbon dioxide, the partial pressures of the two components can be calculated as follows: $p_{CO_2} = \chi \cdot p_{tot}$ and $p_a = (1-\chi) \cdot p_{tot}$. Table 1 shows typical values for the increase in partial pressure of background air as more CO_2 is added to the atmosphere while $p_{I,a}$ is kept fixed. The molar concentration of CO_2 is not linear in the CO_2 inventory, except in the dilute limit, which refers to a condition in which the concentration of a substance is very low, with low particle densities compared to denser regions or sources (Naraschewski et al. 1999).

Total atmospheric CO_2 (10^{18} mol)	p_{I,CO_2} [1] (Pa)	p_{CO_2} [2] (Pa)	p_a [3] (Pa)	p_{tot} (Pa)	Molar concentration [4] (ppmv)
0.0118	10	6.6	$1.000 \cdot 10^5$	$1.000 \cdot 10^5$	66.0
0.118	100	66.0	$1.000 \cdot 10^5$	$1.001 \cdot 10^5$	658.7
1.18	1000	661.3	$1.003 \cdot 10^5$	$1.001 \cdot 10^5$	6547.7
11.8	10^4	6801	$1.032 \cdot 10^5$	$1.1 \cdot 10^5$	$6.18 \cdot 10^4$
118	10^5	$7.95 \cdot 10^4$	$1.21 \cdot 10^5$	$2.00 \cdot 10^5$	$39.7 \cdot 10^4$
1180	10^6	$9.55 \cdot 10^5$	$1.45 \cdot 10^5$	$1.1 \cdot 10^6$	$86.8 \cdot 10^4$
0.0079	7.1	4.5	$1.000 \cdot 10^5$	$1.000 \cdot 10^5$	45
0.071	62.8	40.0	$1.000 \cdot 10^5$	$1.000 \cdot 10^5$	400
0.25	220.1	140.3	$1.000 \cdot 10^5$	$1.001 \cdot 10^5$	1400
1.42	1266.2	809.8	$1.004 \cdot 10^5$	$1.012 \cdot 10^5$	8000

Table 1 Conversion between various characterizations of Earth's atmospheric CO2 content (white cells). Yellow cells represent key ExoCAM inputs used in my study. The figure and caption have been adapted from Pierrehumbert et al. (2011).

[1] p_{I,CO_2} is the surface pressure exerted by CO_2 in the absence of any other gases.

[2] p_{CO_2} is the partial pressure exerted by CO_2 when it is mixed with the background air. The results were computed for $p_{I,a}$ = 105 Pa (105 Pa = 1bar = 1,000 mbar).

[3] p_a is the resulting partial pressure of air in the mixture.

[4] The final column presents the molar concentration of CO_2, which is nearly equivalent to the volumetric mixing ratio for low concentrations.

For this study, the conversion of atmospheric CO_2 concentration from ppmv to partial pressure p_{CO_2}, which is needed as input in ExoCAM, is performed using the equation (5), originating from the following derivation:

From the paragraph above, and as described by Pierrehumbert et al. (2011), we start from the following relations:

$$\chi = \frac{\frac{p_{I,CO_2}}{m_{CO_2}}}{\frac{p_{I,CO_2}}{m_{CO_2}} + \frac{p_{I,a}}{m_a}} \qquad (1)$$

$$p_{tot} = p_{I,CO_2} + p_{I,a} \qquad (2)$$

$$p_{CO_2} = \chi \cdot p_{tot} \qquad (3)$$

$$p_a = (1 - \chi) \cdot p_{tot} \qquad (4)$$

First, we simplify equation (1):

$$\chi = \frac{\frac{p_{I,CO_2}}{m_{CO_2}}}{\frac{p_{I,CO_2}}{m_{CO_2}} + \frac{p_{I,a}}{m_a}} = \frac{\frac{p_{I,CO_2}}{m_{CO_2}}}{\frac{p_{I,CO_2} \cdot m_a + p_{I,a} \cdot m_{CO_2}}{m_{CO_2} \cdot m_a}} = \frac{\frac{p_{I,CO_2} \cdot m_a}{m_{CO_2} \cdot m_a}}{\frac{p_{I,CO_2} \cdot m_a + p_{I,a} \cdot m_{CO_2}}{m_{CO_2} \cdot m_a}} = \frac{p_{I,CO_2} \cdot m_a}{p_{I,CO_2} \cdot m_a + p_{I,a} \cdot m_{CO_2}}$$

Now, we solve for p_{I,CO_2}:

$$p_{I,CO_2} \cdot m_a = \chi \cdot (p_{I,CO_2} \cdot m_a + p_{I,a} \cdot m_{CO_2})$$

$$p_{I,CO_2} \cdot m_a = (p_{I,a} \cdot m_a \cdot \chi) + (p_{I,a} \cdot m_{CO_2} \cdot \chi)$$

$$p_{I,CO_2} \cdot m_a - (p_{I,a} \cdot m_a \cdot \chi) = p_{I,a} \cdot m_{CO_2} \cdot \chi$$

$$p_{I,CO_2} \cdot m_a \cdot (1 - \chi) = p_{I,a} \cdot m_{CO_2} \cdot \chi$$

$$p_{I,CO_2} = \frac{p_{I,a} \cdot m_{CO_2} \cdot \chi}{m_a \cdot (1 - \chi)}$$

Next, we use this relation in the definition of p_{tot} from equation (2):

$$p_{tot} = p_{I,CO_2} + p_{I,a}$$

$$p_{tot} = \frac{p_{I,a} \cdot m_{CO_2} \cdot \chi}{m_a \cdot (1 - \chi)} + p_{I,a}$$

Substitute this expression of p_{tot} in the definition of p_{CO_2} from equation (3):

$$p_{CO_2} = \chi \cdot (\frac{p_{I,a} \cdot m_{CO_2} \cdot \chi}{m_a \cdot (1 - \chi)} + p_{I,a}) \tag{5}$$

Since χ can be calculated from our input ($\chi = ppmv_{CO_2} \cdot 10^{-6}$) and $p_{I,a}$, m_{CO_2} and m_a are known, we can insert them to finish the conversion of atmospheric CO_2 concentration from ppmv to partial pressure of CO_2 p_{CO_2} in bar.
The known constants are as follows:

$$p_{I,a} = 0.999598\ bar \quad \text{(partial pressure of } N_2\text{)}$$

$$m_{CO_2} = 44.01\ g/mol \quad \text{(molecular weight of } \textit{Carbon Dioxide } (CO_2) \text{ (n.d.))}$$

$$m_a = 28.02\ g/mol \quad \text{(molecular weight of } \textit{Nitrogen } (N_2) \text{ (n.d.))}$$

The reverse conversion from p_{CO_2} in bar to ppmv can be performed as follows:

$$p_{ICO_2} = \frac{\sqrt{4 \cdot p_{CO_2} \cdot m_{CO_2} \cdot p_{I,a} \cdot m_a + (p_{CO_2} \cdot m_a - p_{I,a} \cdot m_a)^2} + p_{CO_2} \cdot m_a - p_{I,a} \cdot m_a}{2 \cdot m_a} \tag{6}$$

$$\chi = \frac{\frac{p_{ICO_2}}{m_{CO_2}}}{\frac{p_{ICO_2}}{m_{CO_2}} + \frac{p_{I,a}}{m_a}}$$

$$ppmv_{CO_2} = \chi \cdot 10^6$$

5 Results and Discussion

This chapter presents and analyses the outcomes of my ExoCAM simulations. It is structured as follows: Section 5.1 showcases results for the control run in ExoCAM. Section 5.2 analyses the existence of the waterbelt state in ExoCAM. Section 5.3 discusses the lower bifurcation point. Section 5.4 evaluates the upper bifurcation point, defining the range of a stable waterbelt state, while section 5.5 assesses the CO_2 value at which a temperate, ice-free state transitions to the waterbelt state during ExoCAM simulations and section 5.6 compares the final bifurcation diagrams of ExoCAM with results from other climate models.

5.1 Control run

A control run is initiated with default settings for a CO_2 concentration of 400 ppmv. As with all subsequent runs, the simulation is started at the model date 01/01/00, Northern hemisphere winter time, and is run until a stable ice edge latitude is found.

Figure 8 shows a Hovmöller diagram of the control run, depicting the ice-edge-latitude (by the annual mean of the sea ice fraction) as a function of time. The x-axis denotes latitude, ranging from $-90°$ to $90°$, while the y-axis represents simulated time in years. Each cell in the grid is colored based on the annual mean ice fraction, with blue indicating low ice fraction and white indicating high ice fraction. As anticipated based on the initial conditions outlined in section 4.2, the model starts with an ice edge latitude at $\pm 54°$ and it takes about 20 simulated years for the ice edge latitude to stabilize at $\pm 16°$. For the Southern hemisphere, the ice edge latitude appears to take longer to stabilize, possibly due to the simulation starting during the Southern hemisphere summer. Similarly, figure 9a also portrays the temporal variation in ice edge latitude. It is presented as a line plot of the weighted global mean ice edge latitude as a function of time. The graph commences with the initial conditions of the ice edge latitude at approx. $54°$, after which the curve declines steadily until an ice edge latitude of approximately $\pm 16°$ is reached after approx. 20 simulated years. This value remains stable, with slight variations, for the remaining 80 simulated years. Such representation holds utility for subsequent analysis, as it enables easy comparison between different simulated runs. Weighting is necessary in this context to account for the varying surface area of Earth at different latitudes when computing the mean. By weighting each data point based on its latitude, we ensure that each grid point contributes proportionally to the computed

mean, regardless of its surface area. To accomplish this, the latitude values of the dataset are first converted to radians. Then, the cosine of these radian values is calculated:

```
weights = np.cos(np.deg2rad(data.lat))
weighted_mean = data.weighted(weights).mean(("lon", "lat"))
```

This cosine values represent the weighting factor for each latitude, with higher latitudes receiving less weight due to the cosine function's decrease towards the poles. The simulations are run until they reach a stable state.

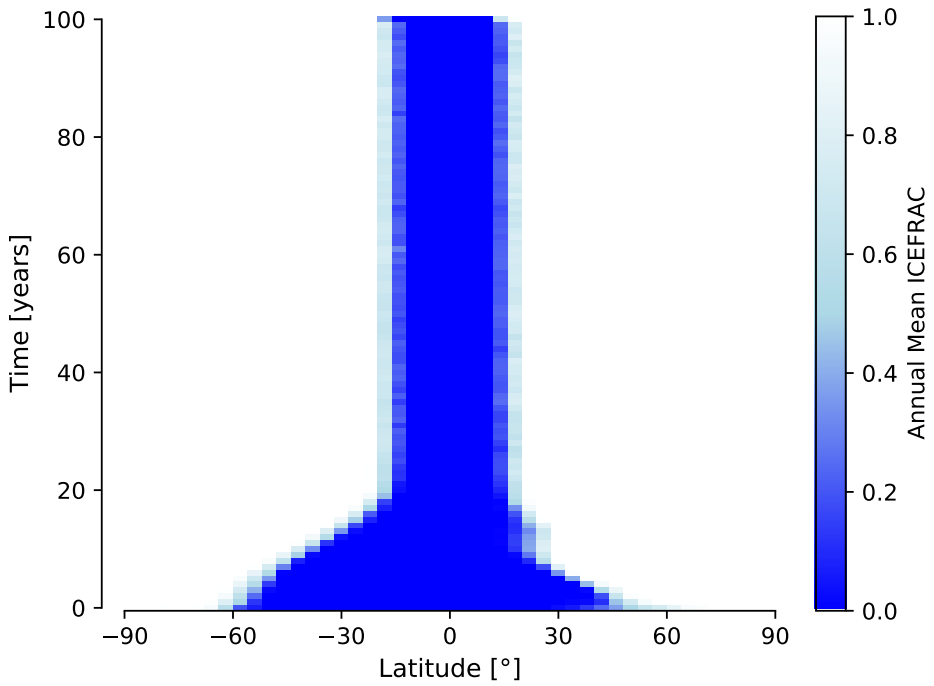

Figure 8 A Hovmöller diagram showcasing the temporal evolution of the ice edge of the control run (400 ppmv CO_2) in ExoCAM across latitudes.

The stability of the system is determined by the change of the energy balance at the top of the atmosphere (TOA) and can be evaluated in figure 9b, which shows the net radiative flux at TOA (in Watts per square-meter) as a function of time. A padded running mean with a window size of 20 years is applied to smooth out the curve. The control run is initiated with values of $-8\mathrm{Wm}^{-2}$, which then increases sharply until it reaches $-2\mathrm{Wm}^{-2}$ after 40 years. For the remaining 60 years, the curve increases steadily from $-2\mathrm{Wm}^{-2}$ to $-1\mathrm{Wm}^{-2}$. Negative values of the TOA net radiative flux indicate a loss of energy of the system, caused by the decreasing ice edge latitude, indicative of the

partial freezing of the ocean. The TOA energy balance is calculated as the difference between net solar flux and net longwave flux at the top of the model. If the imbalance is positive (indicating a surplus of energy entering relative to exiting), energy accumulates within the Earth system, leading to either global warming or cooling should the Earth Energy Imbalance be negative (Von Schuckmann et al. 2023). In this study, a system with relatively small change in TOA net radiative flux (≤ 1 Wm^{-2} in a reasonably large timeframe, such as 50 simulated years) is assumed to be stable. In the case of the control run, at 400 ppmv atmospheric CO_2, the TOA net radiative flux starts at a relatively large negative value of -8 Wm^{-2} subsequently decreases to a stable value between -2 and -1 Wm^{-2}. This result is consistent with negative values indicating a loss in Earth's energy, as the ice edge reaches lower latitudes. Additionally, note that climate models are not strictly energy conserving, as artificial sources and sinks may arise through various model properties.

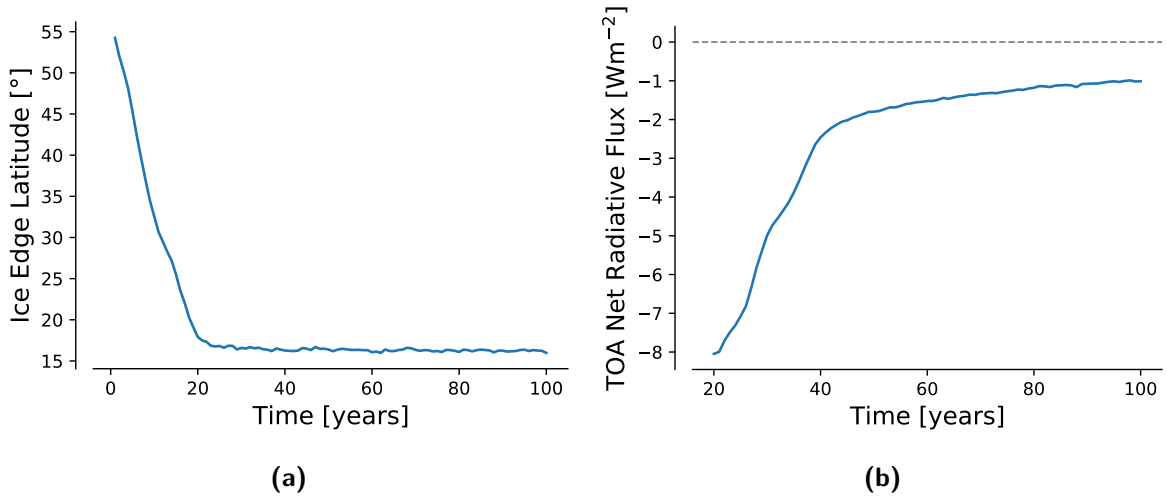

Figure 9 Results for the control run (400 ppmv CO_2) show the temporal evolution of the ice edge latitude of the control run in subplot (a) and the temporal evolution of the top-of-atmosphere (TOA) net radiative flux in subplot (b).

After reaching this stable state, the final ice edge latitude can be plotted against atmospheric CO_2 concentration in a bifurcation diagram for comparison. Results are indicated as a single point in the diagram. If a run starts from initial conditions (a start-up run), it is represented as a diamond, with the control run as an example. Subsequent runs, known as restart or branch runs, are initiated from the final state of a previous simulation rather than from initial conditions and depicted as dots on the bifurcation di-

agram. This technique allows exploring different scenarios using stable states from prior simulations, enabling detailed analysis of the system's response to varying atmospheric CO_2 concentrations. In section 5.3 and subsequent sections, multiple simulated runs are considered in a single bifurcation diagram to assess the geological accessibility of the waterbelt state. Bifurcation points indicate unstable transitions between temperate, waterbelt, and snowball climates (Pierrehumbert et al. 2011).

5.2 Existence of the waterbelt state in ExoCAM

The primary objective is to detect a stable waterbelt state, as its presence is not assured in climate simulations. The control run is set at a default CO_2 value of 0.0004 bar partial atmospheric pressure, which, as described in section 4.3, is equivalent to 399.91 ppmv CO_2 and represents a simulation length of 100 years. Figure 10a displays a Hovmöller diagram of the control run (400 ppmv atmospheric CO_2 concentration). After the initial 100 simulated years, the run is restarted with an increased atmospheric CO_2 concentration of 9400 ppmv and continued until glaciation vanishes globally, which takes an additional 220 simulated years. Similarly, in figure 10b the control run is restarted with a decreased atmospheric CO_2 concentration of 40 ppmv and continued until global glaciation, a snowball Earth, is reached, which takes about 25 additional simulated years.

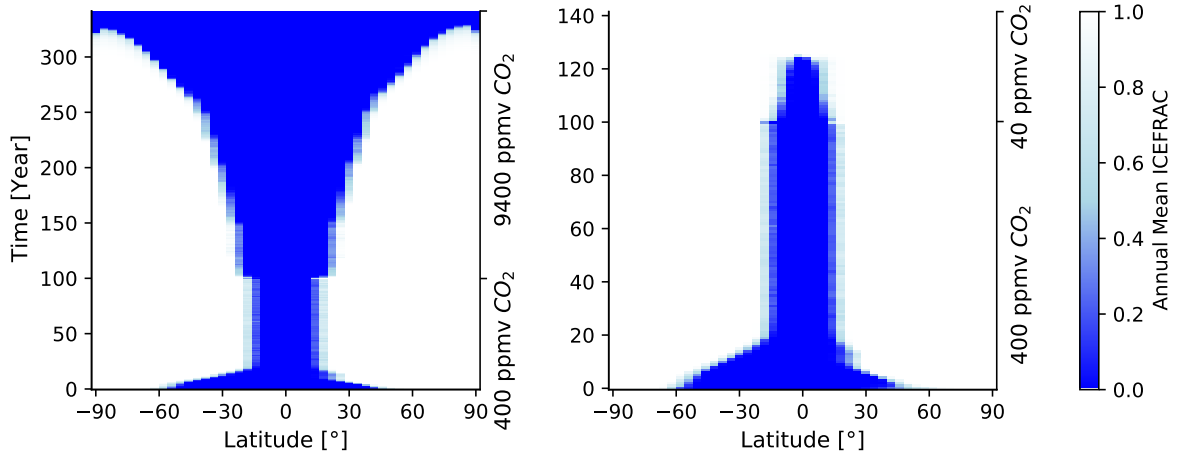

(a) text **(b)** text

Figure 10 Hovmöller diagrams of the control run (400 ppmv CO_2), subsequently restarted with increased (9400 ppmv CO_2 in subplot (a)) and decreased (40 ppmv CO_2 in subplot (b)) atmospheric CO_2 concentration.

This result confirms the existence of a stable waterbelt state using the ExoCAM climate model. In sections 5.3, 5.4 and 5.5 the exact range of atmospheric CO_2 concentrations where this state is stable is evaluated, and its geological accessibility studied.

Characteristics of the waterbelt state in ExoCAM

Upon confirmation of the waterbelt state's existence as outlined in section 5.2, it becomes necessary to examine its characteristics and defining features.

As previously outlined in section 1, Abbot et al. (2011) introduced a novel subcategory of the waterbelt state, designated as the Jormungand state. Contrasting with the depiction of the Jormungand state in CAM presented by Abbot et al. (2011) in figure 3, figure 11 showcases the same diagram using ExoCAM. While both climate simulations feature seasonal sea ice coverage, the ExoCAM results reveal a notably wider region of open ocean. Its results show a maximum latitude of open ocean of approximately 22°, in contrast to the maximum latitude of approximately 11° from figure 3.

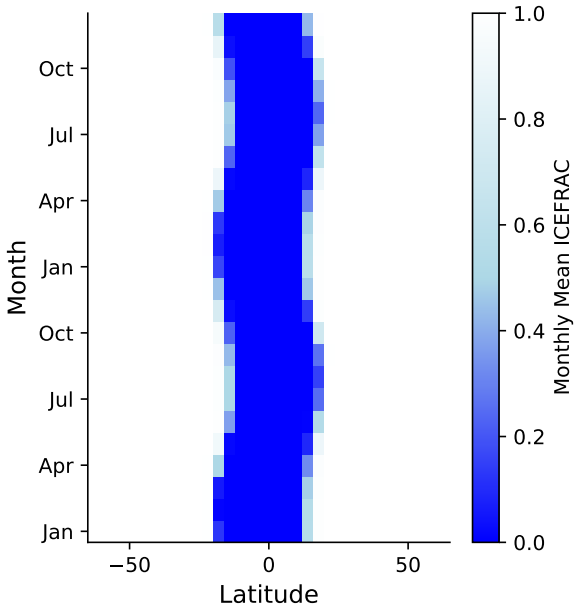

Figure 11 Hovmöller diagram of the zonal mean sea-ice fraction in the waterbelt state with $pCO_2 = 400$ ppmv simulated in ExoCAM. A timespan of 2 years is plotted on the y-axis, showcasing seasonal variability in the ice edge latitude of the waterbelt state.

To investigate the characteristics of the Jormungand state in ExoCAM in more detail, it is necessary to consider the relationship between snow depth over ice, sea ice cover,

and albedo as a function of latitude. Figure 12 illustrates this relationship, demonstrating that snow depth over ice peaks at approximately ±35° with a maximum depth of approximately 7 meters. The snow depth over ice gradually decreases towards the poles on both hemispheres due to the limited supply of precipitation in those regions, reaching approximately 1 meter at the poles. Subsequently, the snow depth over ice decreases steeply equatorward from its peak at ±35°, reaching 0 at approximately ±25° latitude. At this point, the zonal mean of surface area covered by sea ice undergoes a pronounced decline from 1 (total ice coverage at all longitudes) to 0 at the ice edge at ±14° latitude. This approximately 11° wide area, which is highlighted with light blue shading, represents a band of bare sea-ice poleward of the ice edge.

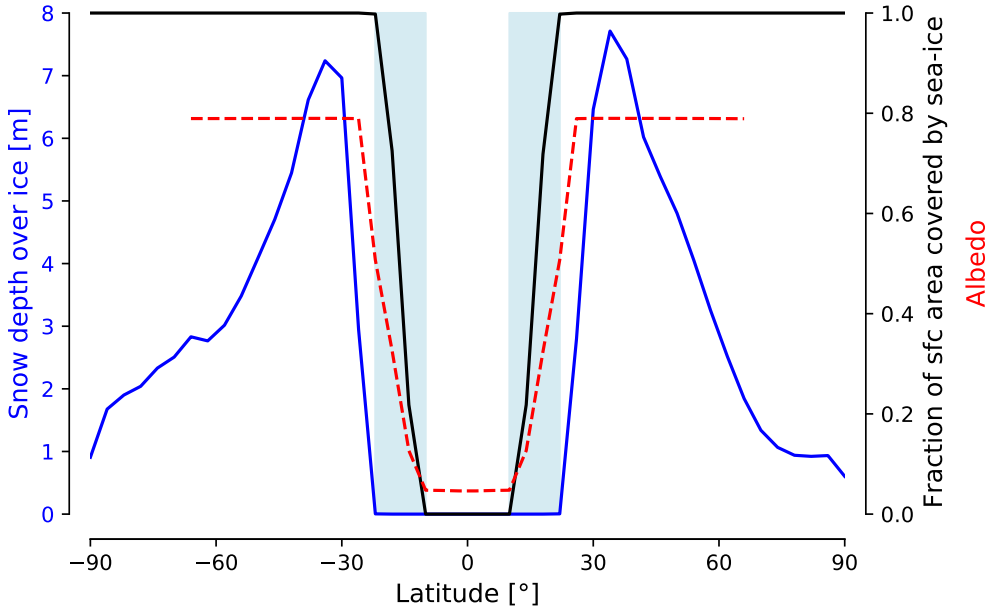

Figure 12 Snow depth over ice, Fraction of surface area covered by sea-ice and albedo plotted against latitude for the control run (400 ppmv CO_2) in ExoCAM.

The albedo values for snow-covered sea ice can be seen at 0.78, while at open ocean it can be found at below 0.1. Figure 13 facilitates an examination of albedo across the region of bare sea ice via a global map. It reveals zonal fluctuations, with albedo values of 0.45 for the transition zone between snow-covered sea ice and open ocean, indicative of bare sea ice.

Based on my findings identifying the main characteristics of the Jormungand state, it can be concluded that the waterbelt state achieved in ExoCAM corresponds to a Jormungand state as described in previous research (Abbot et al. 2011).

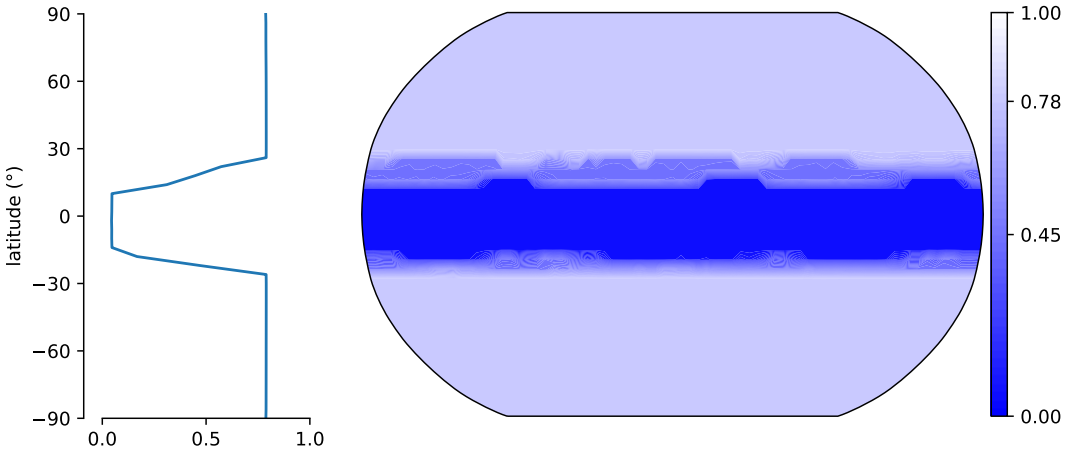

Figure 13 Albedo values of the waterbelt state in ExoCAM plotted as a zonal mean on a global map.

In the Jormungand state, the precipitation minus evaporation (P−E) pattern plays a pivotal role in sustaining this state. In regions where the annual-average P−E value exceeds zero, snow accumulation occurs on sea ice. Conversely, in areas where the annual-average P−E value falls below zero, sea ice remains bare, lacking snow cover for most of the time (Abbot et al. 2011). Figure 14 illustrates the annual and zonal mean P−E for the ice-free and waterbelt states in ExoCAM. Remarkably, these graphs closely resemble those presented in Figure 2b by Abbot et al. (2011), showing peak values at the equator and lowest values around ±10° and ±20° for the waterbelt and ice-free states, respectively. Notably, compared to the waterbelt state, the graph depicting the ice-free state indicates generally higher peaks in both positive and negative directions.

To further assess the impact of clouds on the global climate in ExoCAM, the zonal cloud fraction and its impact on shortwave upward flux reflected by clouds (red line) for the control run are depicted in Figure 15. The shortwave upward flux reflected by clouds is calculated as the difference between the first and last vertical levels of the downward shortwave radiation flux in W/m^2. The cloud fraction reaches its peak of 0.7 at the equator at an altitude of approximately 350 hPa. At approximately ±7°, the clouds reflect the greatest quantity of shortwave flux with up to 170 W/m^2. Polewards, this value drops steeply reaching only 25 W/m^2 at a latitude of ±30°, steadily decreasing towards higher latitudes. This result is anticipated, as solar radiation decreases towards the poles, as well as the underlying sea ice cover reduces the shortwave cloud radiative effect. Additionally, the only source of water vapor necessary for cloud formation is the

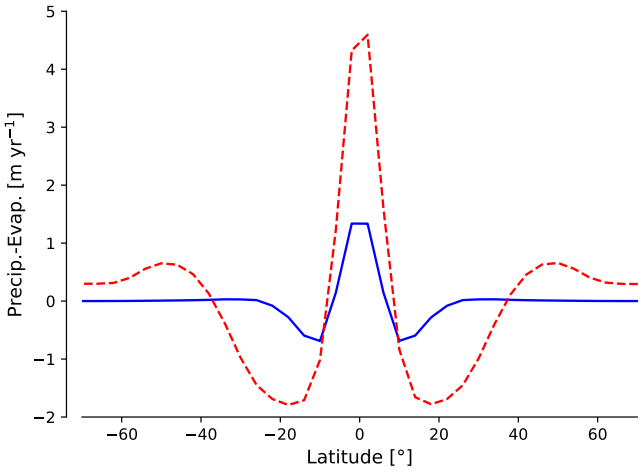

Figure 14 Annual and zonal mean precipitation minus evaporation for the ice-free state (red dashed; 5000 ppmv CO_2) and the waterbelt state (blue; 400 ppmv CO_2). The difference of precipitation minus evaporation is plotted on the y-axis (in myr^{-1}) versus the latitude on the x-axis (in degrees).

open ocean, which, in the waterbelt state, is confined to the equatorial region. The abundant formation of clouds in ExoCAM near the ice edge latitude plays a crucial role in moderating the influence of surface albedo on the top-of-atmosphere albedo, effectively breaking the cycle of the ice-albedo runaway feedback, as described in section 1.

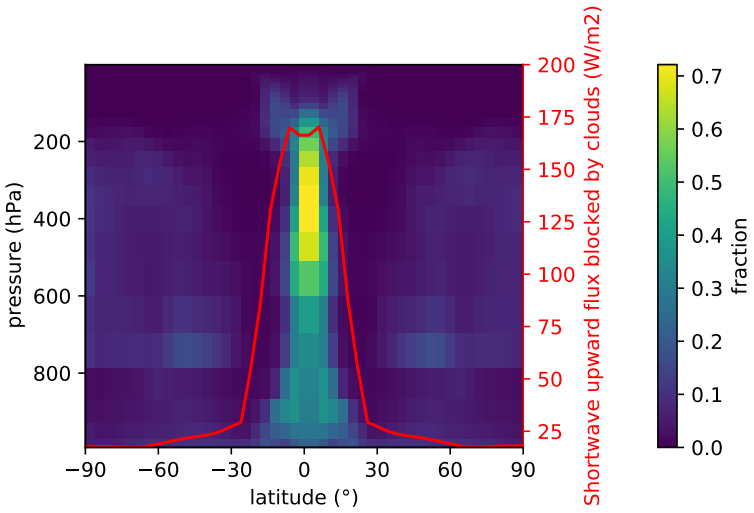

Figure 15 Cloud fraction (colormesh) and its impact on shortwave upward flux blocked by clouds (red line) across latitudes. Lighter regions indicate higher cloud coverage, with peaks at the equator.

The findings examining the attributes of the waterbelt state suggest encouraging indications of a broad and geologically accessible waterbelt state within ExoCAM.

5.3 Lower bifurcation point

In this section, we evaluate the lower bifurcation point discussed in section 1. To locate it, multiple runs with reduced atmospheric CO_2 concentration start as restart runs to the control run. Figure 16 shows the bifurcation diagram with restart runs (dots), as described in section 5.1. The final ice edge latitude of the runs is plotted against their CO_2 concentration. It is evident, that after a sufficient simulated time, a run with 45 ppmv CO_2 is stably sustaining the waterbelt regime, while a run with 40 ppmv CO_2 reaches an ice edge latitude of 0° and therefore global glaciation after about 25 additionally simulated years. The lower bifurcation point, at which any reduction of climate forcing results in the regime changing to a hard snowball Earth event, can therefore be assumed at 45 ppmv atmospheric CO_2 concentration.

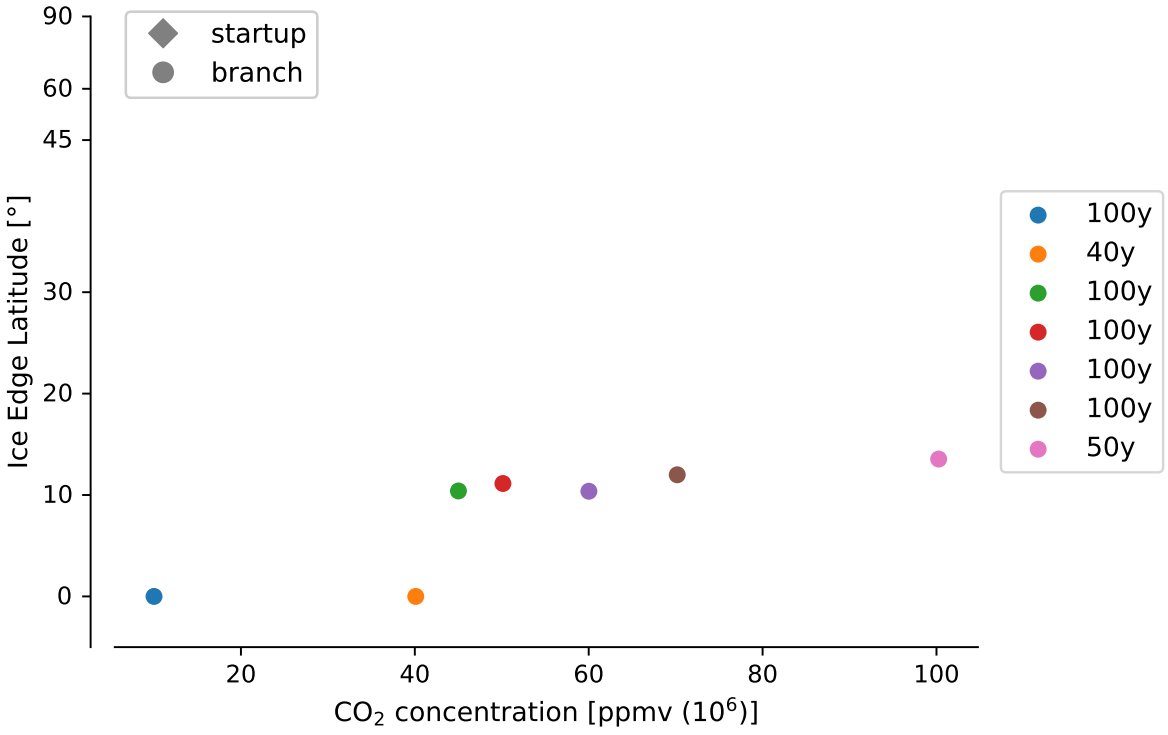

Figure 16 Bifurcation diagram of ExoCAM simulations in search of the lower bifurcation point. The ice edge latitude at the end of a simulated branch run is plotted against the atmospheric CO_2 concentration. The values in the legend represent the simulation duration.

Figure 17 depicts the temporal evolution of multiple simulations with varying CO_2 concentrations. Restart runs continue from the stable ice edge latitude of $\pm 18°$ of the control run. It is evident that runs with slightly lower CO_2 concentration generally result in a slightly lower ice edge latitude, even if they remain stable in the waterbelt regime. The run with the lowest CO_2 concentration (45 ppmv CO_2), while still maintaining a stable waterbelt state, results in a weighted global mean ice edge latitude of approximately $\pm 11°$ after an additional simulation period of 100 simulated years.

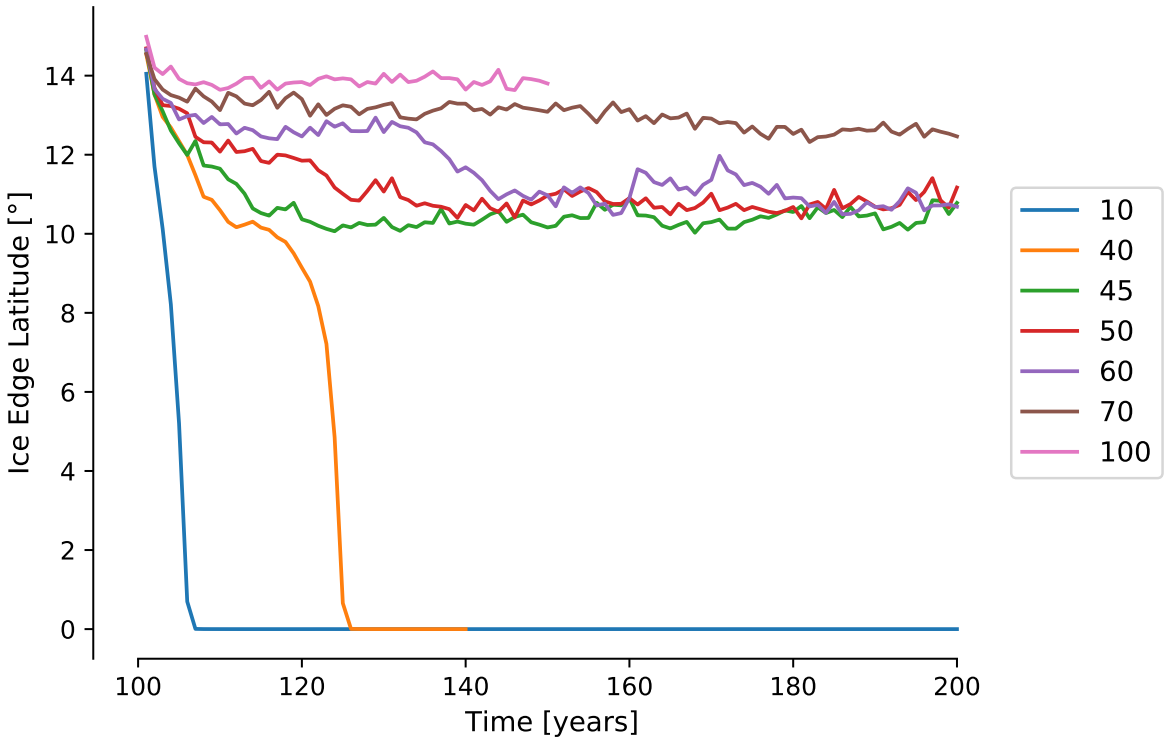

Figure 17 Evolution of the annual-mean ice edge for simulations in search of the lower bifurcation point. The values in the legend represent atmospheric CO_2 concentration in ppmv.

Figure 18 shows the TOA (top of the atmosphere) energy balance for each of the runs close to the lower limit of 45 ppmv CO_2 concentration. Each stable state (45, 50, 60, 70 and 100 ppmv CO_2) represents a relatively small change in TOA net radiative flux ($\leq$ 1 Wm^{-2} in a reasonably large timeframe) with a universal average value of -1 Wm^{-2}, slowly approaching 0 Wm^{-2} over time. Note that inconsistencies at the start and end of the simulations might occur due to the padding method of the running mean, to represent data without the complete coverage of the window size of 20 years. Unstable

runs (10 and 40 ppmv CO_2) show varying values generally between -1 Wm^{-2} and -4 Wm^{-2}, indicating a loss of energy of the planets system through glaciation, as ice edge latitude reaches 0 and a hard snowball Earth with global glaciation is achieved.

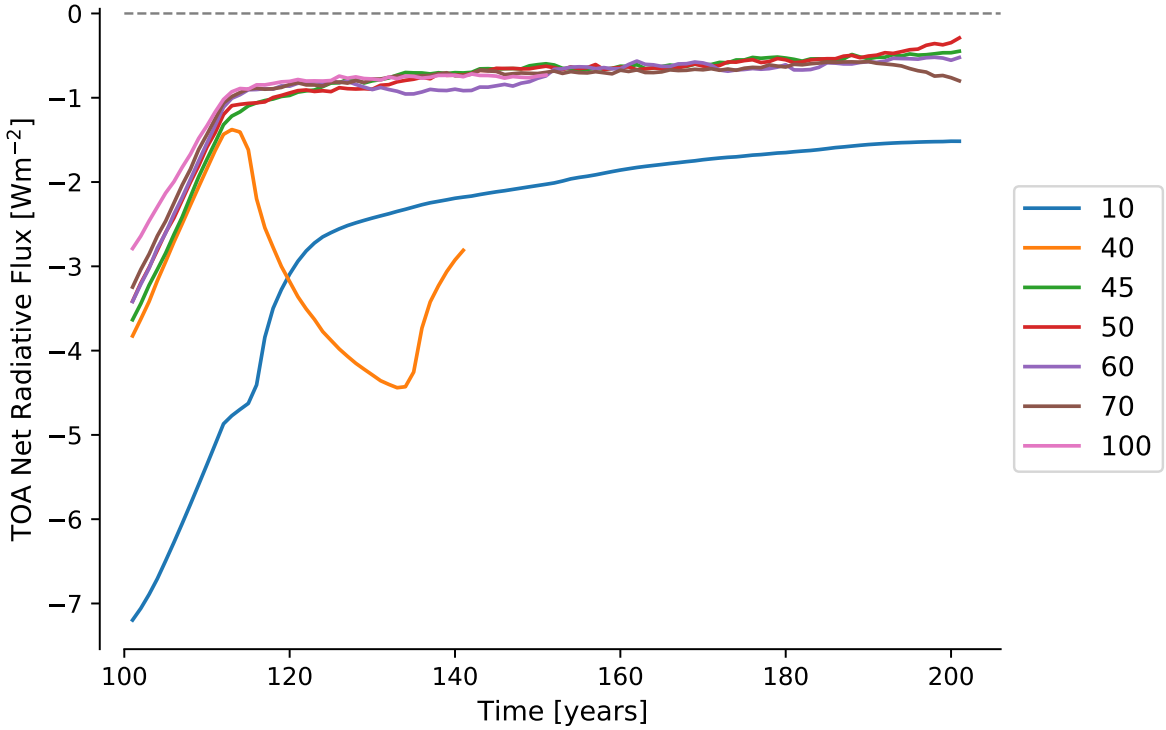

Figure 18 Evolution of the TOA net radiative flux for simulations in search of the lower bifurcation point. The values in the legend represent atmospheric CO_2 concentration in ppmv.

5.4 Upper bifurcation point

Analogous to the previous section, in the following paragraphs we identify the upper bifurcation point, as discussed in section 1. We initiate runs restarted from the control run with increased atmospheric CO_2 concentration, allowing the ice edge latitude to extend to the poles. Figure 19 illustrates the bifurcation diagram of the restart runs with increased CO_2 concentration. The simulations are conducted with an increase of 500 to 1000 ppmv of CO_2 between each representation.

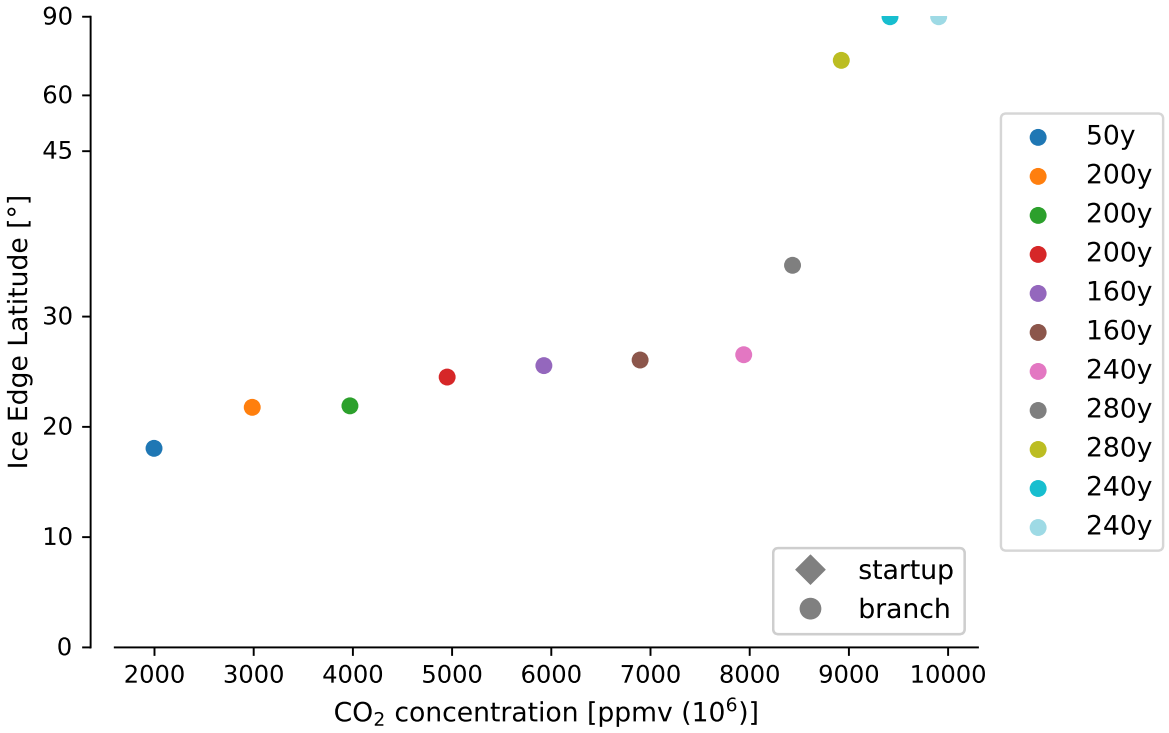

Figure 19 Bifurcation diagram of ExoCAM simulations in search of the upper bifurcation point. The values in the legend represent the simulation duration.

Figure 20 shows the temporal evolution of multiple simulations with different CO_2 concentrations. It is evident that runs with CO_2 concentrations of 8500 and 9000 ppmv are non-stable and indicate deglaciation as the respective values of ice edge latitude approach the poles. The process of deglaciation takes significantly longer compared to glaciation, discussed in section 5.3. The run with an CO_2 increase to 10,000 ppmv reaches an ice edge latitude of 90° and therefore global deglaciation after approximately 200 simulated years after being restarted from the control run. With lower CO_2 concentrations in subsequent runs, deglaciation takes longer. For instance, the run with approximately 9500 ppmv CO_2 reaches an an ice edge latitude of 90° after 231 additional simulated years. The runs with approximately 9000 ppmv and 8500 ppmv were terminated after 280 additional simulated years at ice edge latitudes of 72° and 34°, respectively. Both runs demonstrate evidence of continuous deglaciation. The results of the simulations indicate that runs with CO_2 concentrations below 8500 ppmv show no significant increase in ice edge latitude. However, some runs exhibit certain jumps instead of a steady increase. For instance, a run with a CO_2 concentration of 7000 ppmv exhibits a steady ice edge latitude of 22.7° for approximately 60 simulated years. Subsequently, there is a jump

to 26°, which occurs over a time span of approximately 20 years during which the ice edge latitude increases. The simulation then continues in a steady state at this value for the remaining 80 years. A similar pattern of behaviour can be determined in runs with higher concentrations of CO_2, namely 8000, 8500, and 9000 ppmv. In these cases, the ice edge latitude diverges from a steady state with increasing ice edge latitude values towards the end of the runs.

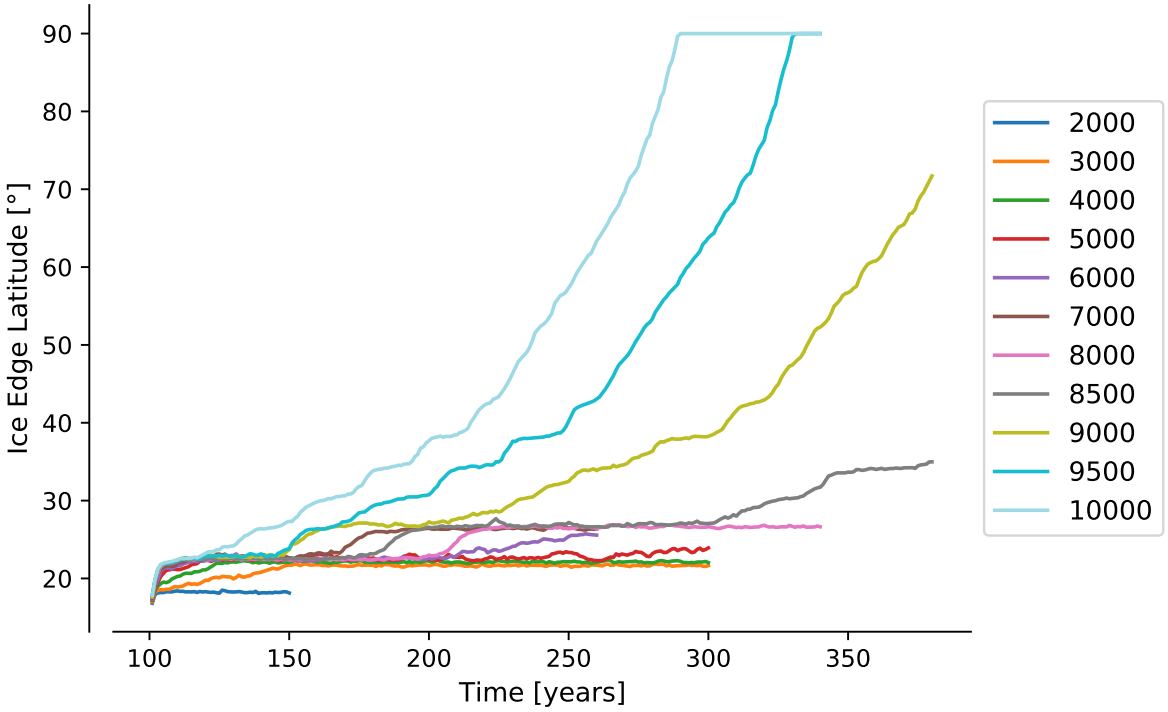

Figure 20 Evolution of the annual-mean ice edge for simulations in search of the upper bifurcation point. The values in the legend represent atmospheric CO_2 concentration in ppmv.

Each of these abrupt changes in ice edge latitude values is detectable in figure 21. This figure shows the TOA energy balance for each of the runs close to the upper limit. These jumps are evident as relatively stable values of TOA net radiative flux of approximately -0.5 Wm^{-2} suddenly peak at $+1$ Wm^{-2} and drop down to their initial values in a time period of approximately 40 simulated years. These peaks align with the time slots of sudden increases of values of ice edge latitude as depicted in figure 20. It should be noted that the window-size of 20 years of data at the boundaries of the simulations are not represented in this plot, as padding of the running mean is disabled here to ensure the consistency of the results between the runs.

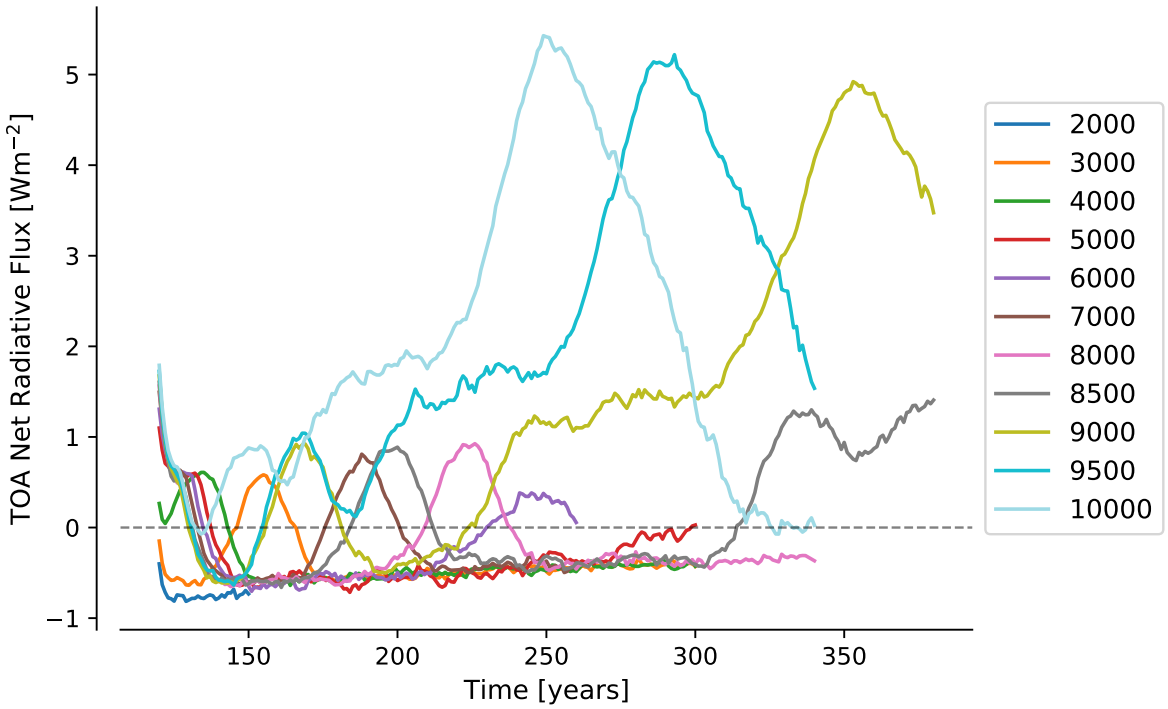

Figure 21 Evolution of the TOA net radiative flux for simulations in search of the upper bifurcation point. The values in the legend represent atmospheric CO_2 concentration in ppmv.

The simulations that result in global deglaciation exhibit positive values of TOA net radiative flux in figure 21, which is indicative of an energy gain for the simulated planet as the ice edge latitude approaches the poles. After the deglaciation event is completed for the run representing 10,000 ppmv CO_2, the TOA net radiative flux approaches 0, indicating a stable balance with neither energy gain nor loss of the planet. Other runs with slightly less CO_2 concentration, that also indicate deglaciation events, appear to follow this trend. Longer run durations would be required to reach certainty. Within the first 240-280 simulated years, the run with the highest CO_2 concentration and a reasonably small change in TOA net radiative flux (≤ 1 Wm^{-2}) is the one representing 8000 ppmv CO_2, which indicates the upper bifurcation point. The timeline of the TOA net radiative flux ranges from approximately -0.8 Wm^{-2} to 0 Wm^{-2} with a steady increase over the 200 simulated years.

5.5 Bifurcation point from ice-free state

In this section, we examine the bifurcation point transitioning from the ice-free (temperate) state, as outlined in section 1. We aim to determine whether the waterbelt state in ExoCAM is geologically accessible. In order to identify an ice-free simulation in which the ice edge latitude stabilizes at the poles, start-up runs with different CO_2 concentrations are initiated. These start-up runs are indicated as diamonds in figure 22. An ice-free simulation is found at a CO_2 concentration of 5000 ppmv. Subsequently, branch runs with a decreased CO_2 concentration are initiated from this ice-free state until instability can be detected.

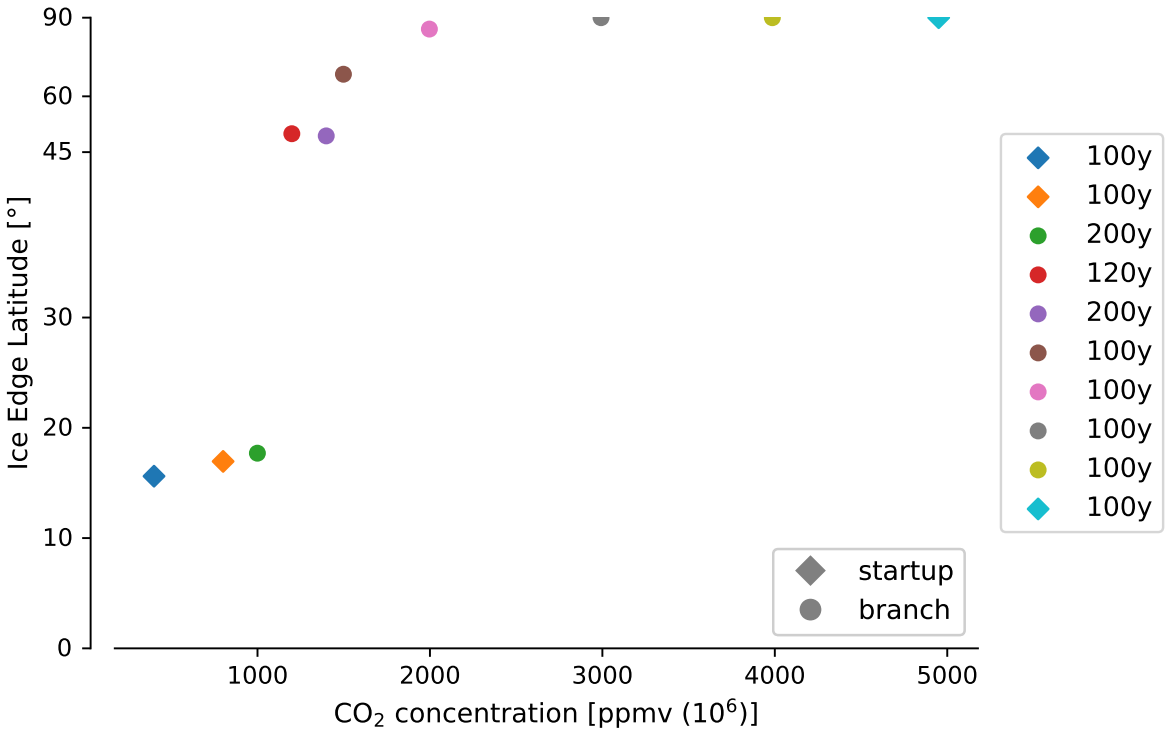

Figure 22 Bifurcation diagram of ExoCAM simulations in search of the bifurcation point from the ice-free state. The values in the legend represent the simulation duration. Dots indicate branch runs restarted from the start-up run in the temperate state (5000 ppmv CO_2) with decreased CO_2 concentration.

Figure 23 shows the temporal evolution of the ice edge latitude of these runs. The startup runs are evidently launched from the initial conditions with an ice edge latitude of approximately 54°; this reaches the waterbelt state and the poles for runs with low (400, 600, 800 ppmv) and high (5000 ppmv) CO_2 concentration, respectively, after 25

simulated years. Branch runs, which are initiated from the ice-free state, exhibit a stable ice edge latitude of 90° down to a CO_2 concentration of approximately 2500 ppmv. Two runs with lower CO_2 concentrations (1500 ppmv and 2000 ppmv) exhibit an ice edge moving equatorward in the initial 20 years, yet ultimately stabilize at ice edge latitudes of 68° and 81°, respectively, over the remaining 80 simulated years. A further decrease in CO_2 concentration to 1000 ppmv inevitably results in sea ice cover reaching the waterbelt state after approximately 75 additional simulated years of glaciation.

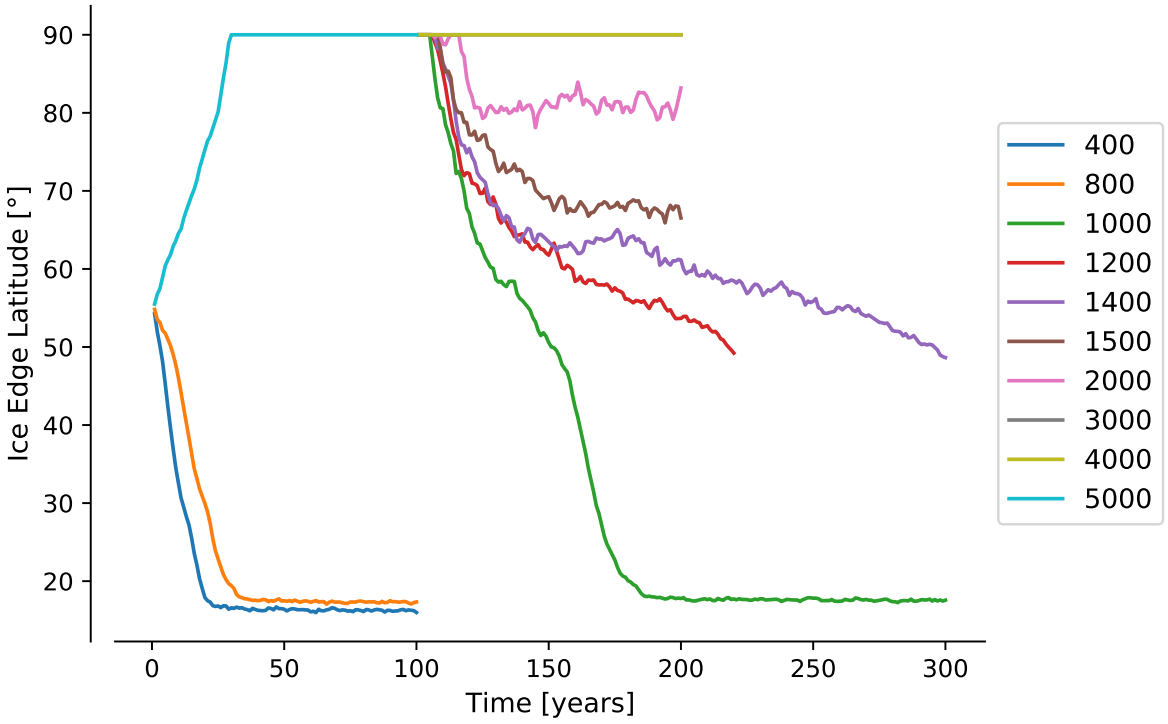

Figure 23 Evolution of the annual-mean ice edge for simulations in search of the bifurcation point from the ice-free state. The values in the legend represent atmospheric CO_2 concentration in ppmv.

Figure 24 illustrates the TOA energy budget for startup and branch runs. Low and high CO_2 startup runs exhibit negative and positive net radiative flux values respectively. The branch run with a CO_2 concentration of 1000 ppmv, which resulted in glaciation until the waterbelt state was reached, exhibited negative values of net radiative flux at TOA with a range of -2 to -6 Wm^{-2}. The remaining branch runs, including the ones which indicate the onset of slight glaciation but ultimately stabilize at different ice edge latitudes, show neutral values of TOA net radiative flux at 0 Wm^{-2} with minimal fluctuation.

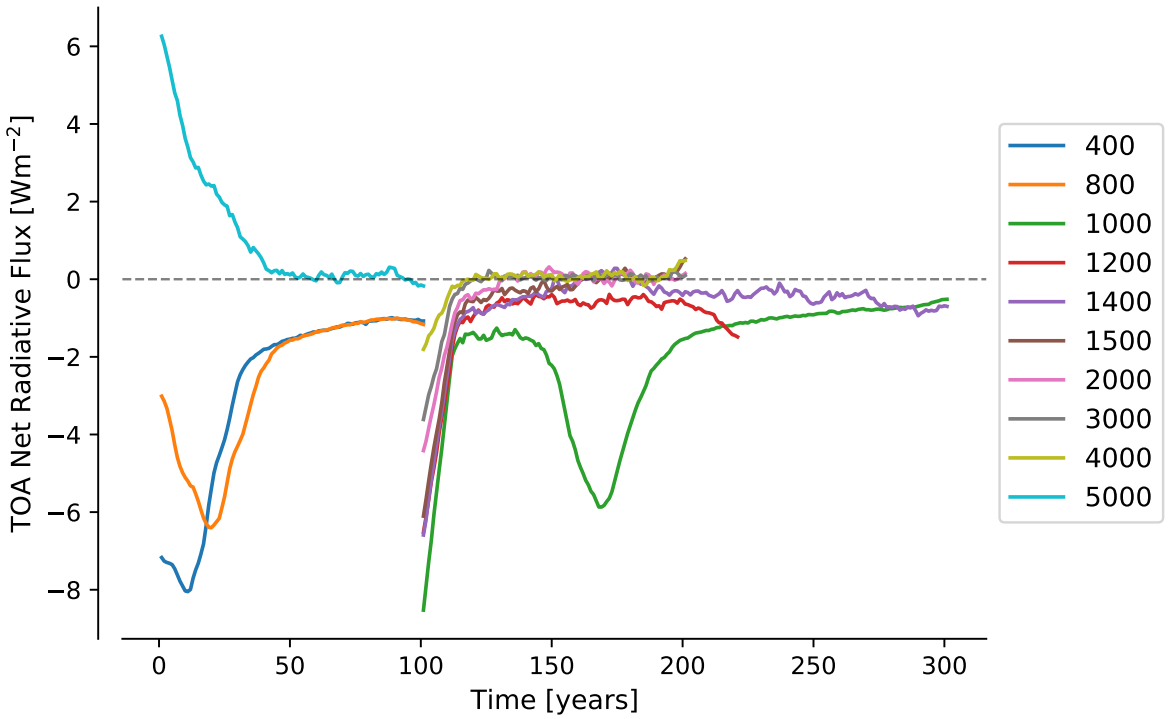

Figure 24 Evolution of the TOA net radiative flux for simulations in search of the bifurcation point from the ice-free state. The values in the legend represent atmospheric CO_2 concentration in ppmv.

This result is indicative of a bifurcation point from the temperate, ice-free state at a CO_2 concentration of approximately 1400 ppmv.

5.6 Comparison: CAM - ICON - ExoCAM

One of the objectives of this study is to gain insight into the range of models that can simulate a geologically plausible waterbelt state. In addition, a direct comparison with other results from previous work is conducted. Therefore, the results from the climate model ExoCAM is evaluated in comparison to those from the climate model CAM, ICON and ICON WBF (Braun et al. 2022), which are discussed in section 1.

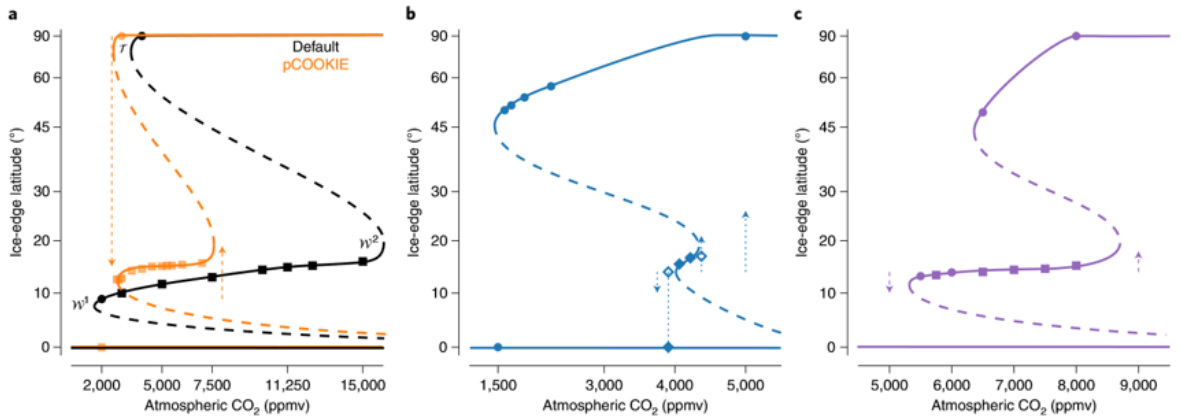

Figure 25 Bifurcation diagrams indicating the existence and absence of waterbelt states in the GCMs CAM and ICON. Subplot (a), (b) and (c) show results from climate models CAM, ICON and ICON WBF, respectively. The figure and caption have been adapted from Braun et al. (2022).

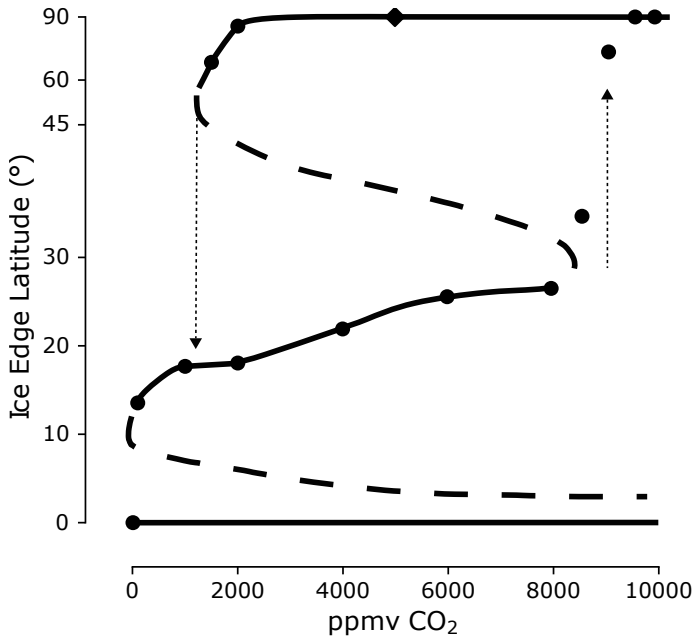

Figure 26 Bifurcation diagram indicating the existence of the waterbelt state in ExoCAM. Each dot represents a simulation conducted in ExoCAM. Solid lines refer to stable states, as dashed lines represent unstable equilibria. Arrows hint at transitions of climate states. The simulations of 8500 and 9000 ppmv CO_2 ended during the transition from the waterbelt state to the temperate state. Consequently, the dots representing these simulations are not situated on a line.

Similar to the preceding three subplots, figure 26 exhibits a bifurcation diagram illustrating the global-mean ice edge latitude relative to atmospheric CO_2 concentration, utilizing results from my investigation employing the ExoCAM climate model. Much like CAM, ExoCAM displays three discernible and stable climate regimes: a temperate regime characterized by minimal or absent ice cover, a waterbelt regime defined by an ice edge positioned between 9° and 15° latitude, and a snowball regime marked by global ice coverage. The critical bifurcation points occur at specific CO_2 concentrations: the lower bifurcation point emerges at 45 ppmv CO_2, the upper threshold is identified at a CO_2 concentration of 8000 ppmv, and the transition from the temperate climate regime occurs at 1400 ppmv CO_2. Table 2 presents the final results of various climate models (including ExoCAM), delineating the waterbelt state via its bifurcation points and the extent of open ocean denoted by the position of the ice edge across latitudes.

Waterbelt State Characteristics				
Model	Lower Bifurcation	Upper Bifurcation	Ice-free Bifurcation	Ice edge range
ExoCAM	45	8000	1400	14° - 22°
CAM	1750	15,000	3000	9° - 15°
ICON	4000	5250	1594	15° - 17°
ICON WBF	1750	8500	6250	13° - 16°

Table 2 Characteristics of the waterbelt state in different climate models. Bifurcation points represent atmospheric CO_2 concentrations in ppmv. The ice edge range shows the lowest and highest latitudes of the waterbelt state. Results for models other than ExoCAM adapted from Braun et al. (2022).

Given that the lower bifurcation point appears at substantially lower CO_2 concentrations compared to the transition point from the temperate climate regime, the waterbelt state is geologically accessible and can be simulated within a wide range, spanning 7955 ppmv CO_2 with the maximum ice edge latitude between a range of 14° and 22° latitude.

6 Conclusion

This thesis explored the climate dynamics of a Snowball Earth, particularly investigating the existence and geological plausibility of waterbelt states using the ExoCAM climate model. In conclusion, I revisit the research question posed in Chapter 2.

How accessible is the waterbelt state in ExoCAM in comparison to CAM and ICON and how geologically plausible is it?

The ExoCAM simulations confirm the existence of a stable waterbelt state. The identification of three bifurcation points (lower, upper, and transition from the ice-free state) provides a comprehensive understanding of the stable range and accessibility of the waterbelt regime in relation to atmospheric CO_2 concentrations. The stable waterbelt state in ExoCAM is found ranging from 45 to 8000 ppmv CO_2. The transition from a temperate, ice-free state begins at 1400 ppmv CO_2, underscoring the geological feasibility of the waterbelt state in ExoCAM.

Furthermore, the characteristics of the waterbelt state exhibit striking resemblance to the Jormungand state identified in prior research. The presence of bare sea ice patches, found in ExoCAM, is pivotal in counteracting the ice-albedo runaway feedback. The seasonal ice edge, from which the Jormungand state draws its name inspired by Norse mythology for its resemblance to the serpent-like structure in hovmöller diagrams, is also evident. The analysis of seasonal ice coverage, albedo variations, and the influence of clouds on incoming solar radiation offers a thorough explanation for the initiation of the waterbelt state in ExoCAM.

Moreover, comparing the representations of waterbelt states in various climate models, specifically CAM, ICON, and ICON WBF, with the results achieved with ExoCAM, reveals the diverse representations across different modelling frameworks. ExoCAM, built upon the CAM framework, produces similar results but demonstrates an even broader and more accessible waterbelt state due to its ability to simulate extensive cloud cover. This characteristic aids to mitigate the dominance of surface albedo in the top-of-atmosphere albedo, thus interrupting the ice-albedo runaway feedback loop.

This thesis has demonstrated promising results in identifying geologically plausible waterbelt states within the ExoCAM climate model, which are critical for enhancing the survivability of life under extreme conditions such as Snowball events. However, the

adjustment of model parameters, including solar irradiation, orbital period, obliquity, eccentricity, atmospheric composition and air pressure, to resemble an Earth-like planet for comparability with previous studies, limits the exploration of a wider range of planetary conditions. As ExoCAM is designed to support extraterrestrial and interstellar objects and is continually expanding to encompass a broader range of environmental factors, future studies could leverage the identified waterbelt states in ExoCAM to investigate the habitability of non-Earth-like planets with greater certainty.

Bibliography

Abbot, Dorian S., Aiko Voigt, and Daniel Koll (2011). "The Jormungand global climate state and implications for Neoproterozoic glaciations". In: 116 (D18), p. D18103. DOI: http://doi.org/10.1029/2011JD015927.

Allen, Philip A. and Paul F. Hoffman (2005). "Extreme Winds and Waves in the Aftermath of a Neoproterozoic Glaciation". In: *Nature* 433, pp. 123–127. DOI: 10.1038/nature03260.

Brady, Patrick V. and Susan A. Carroll (1994). "Direct Effects of CO2 and Temperature on Silicate Weathering: Possible Implications for Climate Control". In: *Geochimica et Cosmochimica Acta* 58, pp. 1843–1856. DOI: 10.1016/0016-7037(94)90502-9.

Braun, Cristoph, Johannes Hörner, and Aiko Voigt (2022). "Ice-free tropical waterbelt for Snowball Earth events questioned by uncertain clouds". In: 15 (6), pp. 489–493. DOI: http://doi.org/10.1038/s41561-022-00950-1.

Carbon Dioxide (CO_2) (n.d.). NIST Chemistry WebBook, SRD 69. National Institute of Standards and Technology. Accessed: 2024-06-14. URL: https://webbook.nist.gov/cgi/cbook.cgi?ID=C124389&Units=SI&Mask=1#MW.

Christie-Blick, Nicholas, Linda E. Sohl, and Martin J. Kennedy (May 1999). "Considering a Neoproterozoic Snowball Earth". In: *Science* 284.5417, pp. 1087–1087. DOI: 10.1126/science.284.5417.1087.

Crowley, Thomas J., William T. Hyde, and W. Richard Peltier (2001). "CO2 Levels Required for Deglaciation of a "Near-Snowball" Earth". In: *Geophysical Research Letters* 28, pp. 283–286. DOI: 10.1029/2000GL011757.

Dohrmann, Martin and Gert Wörheide (2017). "Dating Early Animal Evolution Using Phylogenomic Data". In: *Scientific Reports* 7, p. 3599. DOI: 10.1038/s41598-017-03377-6.

Giorgetta, Marco A. (2018). "ICON-A, the Atmosphere Component of the ICON Earth System Model: I. Model Description". In: 10 (7), pp. 1613–1637. DOI: http://doi.org/10.1029/2017MS001242.

Higgins, John A. and Daniel P. Schrag (2003). "Aftermath of a Snowball Earth". In: *Geochemistry, Geophysics, Geosystems* 4, p. 1028. DOI: 10.1029/2003GC000521.

Hoffman, Paul F., Dorian S Abbot, Yosef Ashkenazy, Douglas I Benn, Jochen J Brocks, Phoebe A Cohen, Grant M Cox, Jessica R Creveling, Yannick Donnadieu, Douglas H Erwin, Ian J Fairchild, David Ferreira, Jason C Goodman, Galen P Halverson, Malte F Jansen, Guillaume Le Hir, Gordon D Love, Francis A Macdonald, Adam

C Maloof, Camille A Partin, Gilles Ramstein, Brian E J Rose, Catherine V Rose, Peter M Sadler, Eli Tziperman, Aiko Voigt, and Stephen G Warren (2017). "Snowball Earth climate dynamics and Cryogenian geology-geobiology". In: 3 (11), e1600983. DOI: http://doi.org/10.1126/sciadv.1600983.

Hoffman, Paul F., Alan J. Kaufman, Galen P. Halverson, and Daniel P. Schrag (1998). "A Neoproterozoic Snowball Earth". In: *Science* 281.5381, pp. 1342–1346. DOI: 10.1126/science.281.5381.1342.

Hoffman, Paul F. and Zheng-Xiang Li (2009). "A Palaeogeographic Context for Neoproterozoic Glaciation". In: *Palaeogeography, Palaeoclimatology, Palaeoecology* 277, pp. 158–172. DOI: 10.1016/j.palaeo.2009.03.034.

Hoffman, Paul F. and Daniel P. Schrag (2002). "The Snowball Earth Hypothesis: Testing the Limits of Global Change". In: *Terra Nova* 14, pp. 129–155. DOI: 10.1046/j.1365-3121.2002.00408.x.

Hörner, Johannes (2022). "Snowball Earth initiation and the thermodynamics of sea ice. Journal of Advances in Modeling Earth Systems". In: 14 (8), e2021MS002734. DOI: http://doi.org/10.1029/2021MS002734.

– (2023). "Waterbelt states controlled by sea-ice thermodynamics". In: DOI: http://doi.org/10.5194/egusphere-egu23-13781.

Hyde, W. T., T. J. Crowley, S. K. Baum, and W. R. Peltier (2000). "Neoproterozoic "Snowball Earth" Simulations with a Coupled Climate/Ice-Sheet Model". In: *Nature* 405.6785, pp. 425–429. DOI: 10.1038/35013005.

International Union of Pure and Applied Chemistry (IUPAC) (2007). *Quantities, Units and Symbols in Physical Chemistry*. 3rd. Cambridge: Royal Society of Chemistry. ISBN: 9780854044337.

Kennedy, Martin J., Bruce Runnegar, Anthony R. Prave, K. H. Hoffmann, and Michael A. Arthur (Dec. 1998). "Two or Four Neoproterozoic Glaciations?" In: *Geology* 26.12, pp. 1059–1063. DOI: 10.1130/0091-7613(1998)026<1059:TOFNG>2.3.CO;2.

Komacek, Thaddeus D. (2019). "The Atmospheric Circulation and Climate of Terrestrial Planets Orbiting Sun-like and M Dwarf Stars over a Broad Range of Planetary Parameters". In: 872 (2), p. 208. DOI: http://doi.org/10.3847/1538-4357/aafb33.

Laskar, J., P. Robutel, F. Joutel, M. Gastineau, A. C. M. Correia, and B. Levrard (2004). "A long-term numerical solution for the insolation quantities of the Earth". In: *Astronomy and Astrophysics* 428.1, pp. 261–285. DOI: 10.1051/0004-6361:20041335.

Le Hir, Guillaume, Gilles Ramstein, Yannick Donnadieu, and Raymond T. Pierrehumbert (2007). "Investigating Plausible Mechanisms to Trigger a Deglaciation from a

Hard Snowball Earth". In: *Comptes Rendus Geoscience* 339.3–4, pp. 274–287. DOI: 10.1016/j.crte.2006.09.002.

Maloof, Adam C. (2010). "Possible animal-body fossils in pre-Marinoan limestones from South Australia". In: 3 (9), pp. 653–659. DOI: http://doi.org/10.1038/ngeo934.

Naraschewski, M. and R. J. Glauber (1999). "Dilute limit and resonance scattering in trapped Bose gases". In: *Physical Review A* 59.6, pp. 4595–4606. DOI: 10.1103/PhysRevA.59.4595.

Nitrogen (N_2) (n.d.). NIST Chemistry WebBook, SRD 69. National Institute of Standards and Technology. Accessed: 2024-06-14. URL: https://webbook.nist.gov/cgi/cbook.cgi?ID=C7727379&Units=SI&Mask=1#MW.

NOAA Earth System Research Laboratory (2024). *Mauna Loa Observatory - Global Monitoring Laboratory*. https://www.esrl.noaa.gov/gmd/ccgg/trends/. Accessed: April 27, 2024.

Pierrehumbert, R.T., Dorian S. Abbot, A. Voigt, and D. Koll (2011). "Climate of the Neoproterozoic". In: 39 (1), pp. 417–460. DOI: http://doi.org/10.1146/annurev-earth-040809-152447.

Pollard, David and James F. Kasting (2005). "Snowball Earth: A Thin-Ice Solution with Flowing Sea Glaciers". In: *Journal of Geophysical Research* 110, p. C07010. DOI: 10.1029/2004JC002525.

Rasmussen, Tine L., Christof Pearce, Katrine Juul Andresen, Tove Nielsen, and Marit-Solveig Seidenkrantz (2022). "Northeast Greenland: ice-free shelf edge at 79.4°N around the Last Glacial Maximum 25.5-17.5 ka". In: *Boreas* 51.4, pp. 759–775. DOI: https://doi.org/10.1111/bor.12593. eprint: https://onlinelibrary.wiley.com/doi/pdf/10.1111/bor.12593.

Reinsel, Gregory C and Rolf D Reitz (2008). "Padded running mean smoothing of noisy data using convolutional filters". In: *Journal of Chromatography A* 1209, pp. 126–132. DOI: 10.1016/j.chroma.2008.09.009.

Rodehacke, Christian B., Antje Voigt, Florian Ziemen, and Dorian S. Abbot (2013). "An Open Ocean Region in Neoproterozoic Glaciations Would Have to Be Narrow to Allow Equatorial Ice Sheets". In: *Geophysical Research Letters* 40, pp. 5503–5507. DOI: 10.1002/grl.51082.

Rose, Brian E. J. (2015). "Stable 'Waterbelt' Climates Controlled by Tropical Ocean Heat Transport: A Nonlinear Coupled Climate Mechanism of Relevance to Snowball Earth". In: *Journal of Geophysical Research: Atmospheres* 120, pp. 1404–1423. DOI: 10.1002/2014JD022752.

Storelvmo, Trude and Ivy Tan (2015). "The Wegener–Bergeron–Findeisen Process—Its Discovery and Vital Importance for Weather and Climate". In: *Meteorologische Zeitschrift* 24, pp. 455–461. DOI: 10.1127/metz/2015/0651.

Vertenstein, M. (2013). *CESM user's guide (CESM1.2 release series user's guide)*. NCAR Tech. URL: https://www2.cesm.ucar.edu/models/cesm1.2/cesm/doc/usersguide/book1.html.

Von Schuckmann, Karina, Audrey Minière, Flora Gues, Francisco José Cuesta-Valero, and Gottfried Kirchengast (2023). "Heat stored in the Earth system 1960–2020: where does the energy go?" In: 15 (4), pp. 1675–1709. DOI: http://doi.org/10.5194/essd-15-1675-2023.

Wolf, Eric T., Ravi Kopparapu, Jacob Haqq-Misra, and Thomas J. Fauchez (2022). "ExoCAM: A 3D Climate Model for Exoplanet Atmospheres". In: 3 (1), p. 7. DOI: http://doi.org/10.3847/PSJ/ac3f3d.